Article:
Emrich-Mills, Tom Z, Proctor, Matthew S, Degen, Gustaf E et al. (2025) Tethering ferredoxin-NADP+ reductase to photosystem I promotes photosynthetic cyclic electron transfer. The Plant Cell. koaf042. ISSN: 1532-298X

https://doi.org/10.1093/plcell/koaf042

THE PLANT CELL

The Plant Cell, 2025, **37**, koaf042

https://doi.org/10.1093/plcell/koaf042
Advance access publication 3 March 2025
Research Article

Tethering ferredoxin-NADP$^+$ reductase to photosystem I promotes photosynthetic cyclic electron transfer

Tom Z. Emrich-Mills,[1,†] Matthew S. Proctor,[1,†] Gustaf E. Degen,[1,†] Philip J. Jackson,[1,2] Katherine H. Richardson,[1] Frederick R. Hawkings,[1,3] Felix Buchert,[4] Andrew Hitchcock,[1] C. Neil Hunter,[1] Luke C.M. Mackinder,[5] Michael Hippler,[4,6] Matthew P. Johnson[1,*]

[1]Plants, Photosynthesis & Soil, School of Biosciences, University of Sheffield, Sheffield S10 2TN, UK
[2]Department of Chemical and Biological Engineering, University of Sheffield, Sheffield S1 4LZ, UK
[3]Electron Bio-Imaging Centre, Diamond Light Source, Didcot OX11 0DE, UK
[4]Institute of Plant Biology and Biotechnology, University of Münster, Münster 48149/48143, Germany
[5]Department of Biology, University of York, York YO10 5DD, UK
[6]Institute of Plant Science and Resources, Okayama University, Kurashiki 710-0046, Japan
*Author for correspondence: matt.johnson@sheffield.ac.uk
[†]These authors contributed equally.
The author responsible for distribution of materials integral to the findings presented in this article in accordance with the policy described in the Instructions for Authors (https://academic.oup.com/plcell/pages/General-Instructions) is: Matthew P. Johnson (matt.johnson@sheffield.ac.uk).

Abstract

Fixing CO_2 via photosynthesis requires ATP and NADPH, which can be generated through linear electron transfer (LET). However, depending on the environmental conditions, additional ATP may be required to fix CO_2, which can be generated by cyclic electron transfer (CET). How the balance between LET and CET is determined remains largely unknown. Ferredoxin-NADP$^+$ reductase (FNR) may act as the switch between LET and CET, channeling photosynthetic electrons to LET when it is bound to photosystem I (PSI) or to CET when it is bound to cytochrome b_6f. The essential role of FNR in LET precludes the use of a direct gene knock-out to test this hypothesis. Nevertheless, we circumvented this problem using clustered regularly interspaced short palindromic repeats (CRISPR)/CRISPR-associated nuclease 9 (Cas9)-mediated gene editing in *Chlamydomonas reinhardtii*. Through this approach, we created a chimeric form of FNR tethered to PSI via PSAF. Chimeric FNR mutants exhibited impaired photosynthetic growth and LET along with enhanced PSI acceptor side limitation relative to the wild type due to slower NADPH reduction. However, the chimeric FNR mutants also showed enhanced ΔpH production and NPQ resulting from increased CET. Overall, our results suggest that rather than promoting LET, tethering FNR to PSI promotes CET at the expense of LET and CO_2 fixation.

Introduction

Photosynthesis is essential to life on Earth, converting solar energy into biomass which sustains global food chains, while generating oxygen as a byproduct. The first steps of oxygenic photosynthesis take place in the chloroplast thylakoid membrane. Here, specialized light harvesting complexes (LHCs) absorb solar energy and transfer the excitation to the photosystem I and II (PSI, PSII) reaction centers, where photochemistry takes place (Nelson and Junge 2015). PSII uses the excitation energy to split water into protons and electrons and reduce plastoquinone (PQ) to plastoquinol (PQH_2). PQH_2 is then oxidized by the cytochrome b_6f (cytb_6f) complex which reduces plastocyanin (PC) in the thylakoid lumen (Malone et al. 2021). The protons liberated by cytb_6f and PSII contribute to the proton motive force (pmf) across the thylakoid membrane, which is utilized by ATP synthase to power the endergonic formation of ATP (Kühlbrandt 2019). PSI uses excitation energy to oxidize PC and reduce ferredoxin (FD). Electrons from FD are utilized in linear electron transfer (LET) by the enzyme FD-NADP$^+$ reductase (FNR) to reduce NADP$^+$ to NADPH, which in turn is used to reduce 1,3-bisphosphoglycerate during the CO_2-fixing Calvin–Benson–Bassham (CBB) cycle. Alternatively, electrons from FD or NADPH can re-enter the photosynthetic electron transfer chain to reduce PQ to PQH_2, via cyclic electron transfer (CET) (Yamori and Shikanai 2015; Nawrocki et al. 2019b). In the model eukaryotic green alga *Chlamydomonas reinhardtii*, several other alternative electron transfer pathways also contribute to the chloroplast pmf and so the ATP/NADPH balance (Burlacot 2023). These include the pseudo-cyclic electron transfer (PCET) via the flavodiiron proteins (FLVA and FLVB), which use FD to reduce O_2 to water (Chaux et al. 2017; Setif et al. 2020). Alternatively, reductant may be exported from the chloroplast and consumed in the mitochondria via respiratory electron transfer (RET) (Cardol et al. 2009; Dang et al. 2014). The ATP produced via RET can then be imported into the chloroplast, possibly via the triose phosphate translocator (Alric and Johnson 2017). Each of these pathways makes varying contributions to the pmf and ATP/NADPH balance depending on environmental conditions (Burlacot et al. 2022). Moreover, since they produce pmf, they are also crucial to modulation of ΔpH-dependent photoprotection of PSII, via non-photochemical quenching (NPQ) of

Received July 16, 2024. Accepted February 25, 2025

excess excitation energy, and of PSI, via photosynthetic control (PCON) (Murchie and Ruban 2020; Degen and Johnson 2024).

In Chlamydomonas, two mechanisms of CET have been shown to exist, one mediated by the non-proton-pumping type II NADPH dehydrogenase (NDA2) complex (Desplats et al. 2009), and another that is FD-dependent (Alric et al. 2010; Alric 2014). A leading contender for the role of the FD-dependent plastoquinone reductase (FQR) was the complex formed between the Proton Gradient Regulation Like 1 (PGRL1) and Proton Gradient Regulation 5 (PGR5) proteins (Munekage et al. 2004; DalCorso et al. 2008; Tolleter et al. 2011; Johnson et al. 2014). However, it was later shown that PGRL1 is not essential for CET in either Chlamydomonas or Arabidopsis (Nawrocki et al. 2019a; Rühle et al. 2021). Moreover, the proposed thiol-based interaction between PGRL1 and PGR5 was also not required for functional CET (Buchert et al. 2020). Enhanced CET activity can be measured in Chlamydomonas under low CO_2, which increases ATP demand to fuel the carbon concentrating mechanism (CCM), and under low oxygen conditions (anoxia), which suppress PCET and RET (Lucker and Kramer 2013; Clowez et al. 2015; Burlacot et al. 2022). Anoxia and low CO_2 promote reduction of $NADP^+$ thus lowering the redox potential of the chloroplast stroma and triggering reduction of the PQ pool (Johnson and Alric 2012). In Chlamydomonas, PQ reduction promotes the phosphorylation of PSII light harvesting antenna proteins (LHCII) by the state transition thylakoid protein kinase 7 (STT7), which detach from PSII and become associated with PSI (State II) (Depège et al. 2003; Nawrocki et al. 2015). The reverse transition to State I is promoted by oxidation of the PQ pool and is catalyzed by the chloroplast protein phosphatase 1 (PPH1) and PSII core phosphatase (PBCP) (Cariti et al. 2020). Biochemical analysis correlated anoxia with the appearance of a high molecular weight supercomplex containing not only PSI and LHCII but also cytb_6f, its weakly bound auxiliary subunit PETO, Anaerobic Response 1 (ANR1), Calcium Sensor Kinase (CAS), PGRL1, and FNR (Iwai et al. 2010; Terashima et al. 2012; Takahashi et al. 2013). If NADPH and FD were added to this supercomplex preparation, the *b*-type hemes associated with the PQ reduction site in cytb_6f were efficiently reduced, suggesting that cytb_6f-tethered FNR mediates FQR activity (Iwai et al. 2010). Recently, it was shown that under anoxic conditions, the oxidation of the *b*-type hemes in cytb_6f is accelerated in a PGR5-dependent fashion (Buchert et al. 2020). Since PGR5 affects the tethering of FNR to the thylakoid membrane, it was suggested to modulate the CET activity of cytb_6f (Mosebach et al. 2017). In this model, the location of FNR therefore decides the fate of electrons emanating from PSI, with soluble or PSI bound FNR mediating LET, while cytb_6f bound FNR mediates CET (Joliot and Johnson 2011). In Arabidopsis, FNR tethering to the thylakoid membrane via TROL and TIC62 complexes was shown to promote CET, however these proteins are absent from Chlamydomonas (Kramer et al. 2021). Moreover, since the putative CET supercomplex is extremely fragile, to date, only a low-resolution structure exists and no information on the precise interactions between FNR, PSI, and cytb_6f exist to clarify the mechanism (Buchert et al. 2018; Steinbeck et al. 2018). Indeed, controversy remains since isolated FNR has itself been shown to possess FQR activity (Bojko et al. 2003), while it has also been suggested that FD could donate electrons directly to cytb_6f in the absence of FNR (Nawrocki et al. 2019b). Therefore, new approaches are required to resolve the outstanding questions regarding the role of FNR location and membrane binding on the balance between LET and CET in Chlamydomonas.

Unfortunately, due to the essential nature of FNR for both autotrophic and heterotrophic (e.g. in nitrogen and fatty acid metabolism (Terauchi et al. 2009)) growth in Chlamydomonas, it has not been possible to test whether its interaction with cytb_6f is a prerequisite for CET. To address this issue, we produced a chimeric *FNR-PSAF* gene encoding a fusion protein that would ensure tethering of FNR to PSI, while simultaneously disrupting the native *FNR* and *PSAF* genes, generating a Chlamydomonas mutant where the only FNR present is the chimeric protein. Unexpectedly, the PSAF-FNR chimeric mutants show enhanced CET compared to the wild-type UVM4 (WT) and restricted LET under high CO_2 conditions. Our results therefore confirm the key role of FNR location in determining the fate of photosynthetic electrons between CET and LET, though exclude the necessity for FNR binding to cytb_6f in the mechanism of CET.

Results

Creation of a chimeric PSAF-FNR protein in Chlamydomonas

To achieve our goal of selectively tethering FNR to PSI, we began by designing a chimeric protein where FNR is fused to the stromal facing C-terminus of the PSI subunit PSAF using a small 9 amino acid linker sequence (Fig. 1A). The plasmid also contains an *AphVIII* selection marker, allowing selection of transformants on paromomycin (Li et al. 2016). The gene encoding the PSAF-FNR chimera was then introduced via CRISPR-Cas9 gene editing to the WT native nuclear *PSAF* locus disrupting the gene. The independent mutant lines created, native/tethered 4 (NT)4 and NT12, contained both native *FNR* and chimeric *PSAF-FNR* genes (Fig. 1B) and the corresponding proteins (Fig. 1, C and D). The NT4 and NT12 mutant lines were then further modified using CRISPR-Cas9 to inactivate the native *FNR* gene by inserting an *AphVII* hygromycin resistance cassette (Fig. 1E), producing the stable independent lines tethered-only (T)7 and T10. Immunoblotting with anti-PSAF and anti-FNR antibodies confirmed that the T7 and T10 mutant cell lines lacked the native PSAF and FNR proteins and contained only the PSAF-FNR chimeric protein at ~53 kDa (Fig. 1, F and G). The whole cell immunoblots also confirmed that the chimeric PSAF-FNR protein was remarkably resistant to proteolytic cleavage to yield free FNR or PSAF in the mutants (Fig. 1, F and G). Nevertheless, we also took the NT12 and NT4 mutants forward as controls for the effect of free FNR in combination with chimeric PSAF-FNR in our subsequent experiments.

Chlamydomonas mutants expressing the PSAF-FNR chimeric gene show inhibited photoautotrophic growth

We next assessed the photoautotrophic growth of the mutants vs. the WT at a light intensity of 60 μmol photons m^{-2} s^{-1} using 14 h/10 h light-dark cycle and atmospheric CO_2 as the sole carbon source (tris-phosphate [TP] medium) (Fig. 2A). The T7, T10, NT4, and NT12 mutants all showed increased doubling time compared to the WT (Fig. 2, A and B). In contrast, photomixotrophic growth under the same light conditions, while employing acetate as the carbon source, was unaffected (tris-acetate-phosphate [TAP] medium) (Fig. 2, A and C). This suggests that the lesion caused by the introduction of the chimera affects photosynthetic electron transfer in such a way as to impede the efficient assimilation of CO_2. In line with this, we recorded a lower rate of PSII electron transfer (ETRII) in the mutants compared to the WT in photoautotrophically grown cultures, even when cells were supplied with a saturating amount (10 mM) of sodium bicarbonate (Fig. 2D).

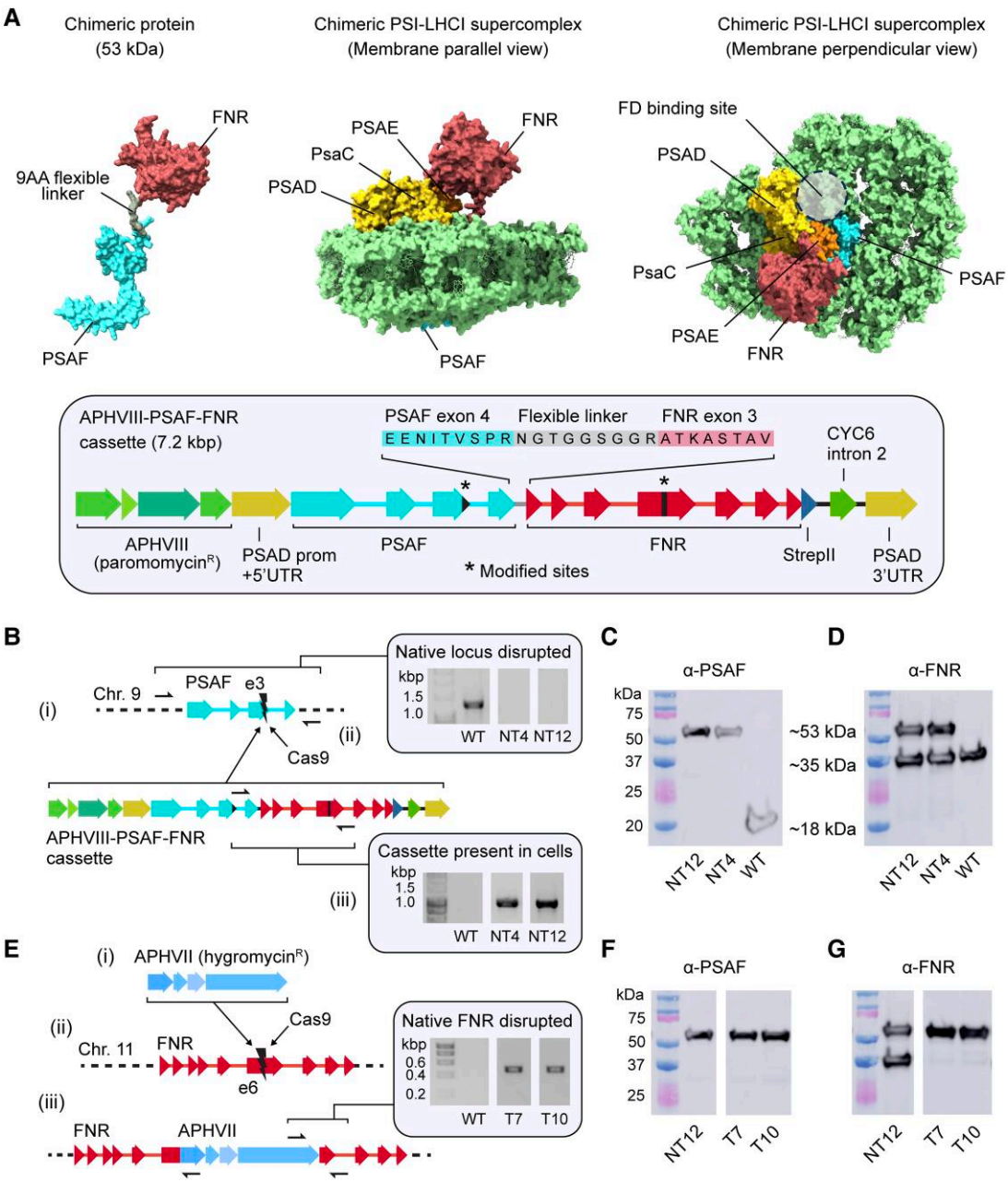

Figure 1. Creation of chimeric PSAF-FNR mutants in Chlamydomonas. **A)** Putative molecular model of the PSAF-FNR chimeric PSI–LHCI complex. The inset below shows a map of the expression cassette for the chimeric protein, along with the amino acid sequence of the linker region. Modified sites refer to silent mutations made in *PSAF* exon 3 and *FNR* exon 6 to avoid CRISPR targeting. **B)** Results of the co-transformation of WT with the *PSAF-FNR* expression cassette and Cas9-single-guide RNA ribonucleoprotein (RNP) targeting *PSAF* exon 3. (i) shows the intended outcome of CRISPR-guided insertional mutagenesis, in which the *PSAF-FNR* expression cassette is inserted into native *PSAF* exon 3 as part of the nonhomologous end joining (NHEJ) repair process. (ii) shows colony PCRs with transformant lines NT4 and NT12. Absence of an amplicon across the *PSAF* locus indicated a large insertion at exon 3; the black arrows indicate the priming sites used to detect this amplicon by PCR. (iii) shows successful amplification using primers specific to the *PSAF-FNR* cassette in lines NT4 and NT12, which indicated successful integration of the cassette into the genome. **C)** Immunoblots with anti-PSAF antibody confirmed deletion of native PSAF in NT4 and NT12. **D)** Immunoblots with an anti-FNR antibody confirmed expression of the PSAF-FNR protein along with native FNR. **E)** Results of the CRISPR-mediated deletion of native *FNR*. (i) shows the *AphVII* cassette used for transformation, encoding resistance to hygromycin. The intention was to select for insertion of *AphVII* into native *FNR* exon 6 (ii) as part of the NHEJ repair process. (iii) shows the intended result, along with evidence of successful PCR amplification across the boundary between native *FNR* and *AphVII* using a 3-primer PCR that allowed for insertion of *AphVII* in either orientation. Amplicons in transformant lines T7 and T10 are strong evidence of correct insertion. **F)** T7 and T10 immunoblots using anti-PSAF and **G)** anti-FNR antibodies indicate loss of native FNR and the presence of the PSAF-FNR chimera. Note that the marker lane and first lane in panels **C)** and **F)** are the same image; likewise, the marker lane and first lane in panels **D)** and **G)** are the same, as the samples were run on the same gel. WT, wild-type; NT4, native/tethered line 4; NT12, native/tethered line 12; T7, tethered-only line 7; T10, tethered-only line 10.

Mutant cells with the chimeric PSAF-FNR protein are shifted to State II

We next confirmed that the chimeric PSAF-FNR protein was stably incorporated into PSI by purifying thylakoids from the NT12 and T7 mutants, solubilizing them with the detergent lauryl maltose neopentyl glycol (LMNG) and separating the complexes via sucrose gradient ultracentrifugation (Fig. 3A). The WT showed 4 major bands on the gradients, consistent with past studies, belonging

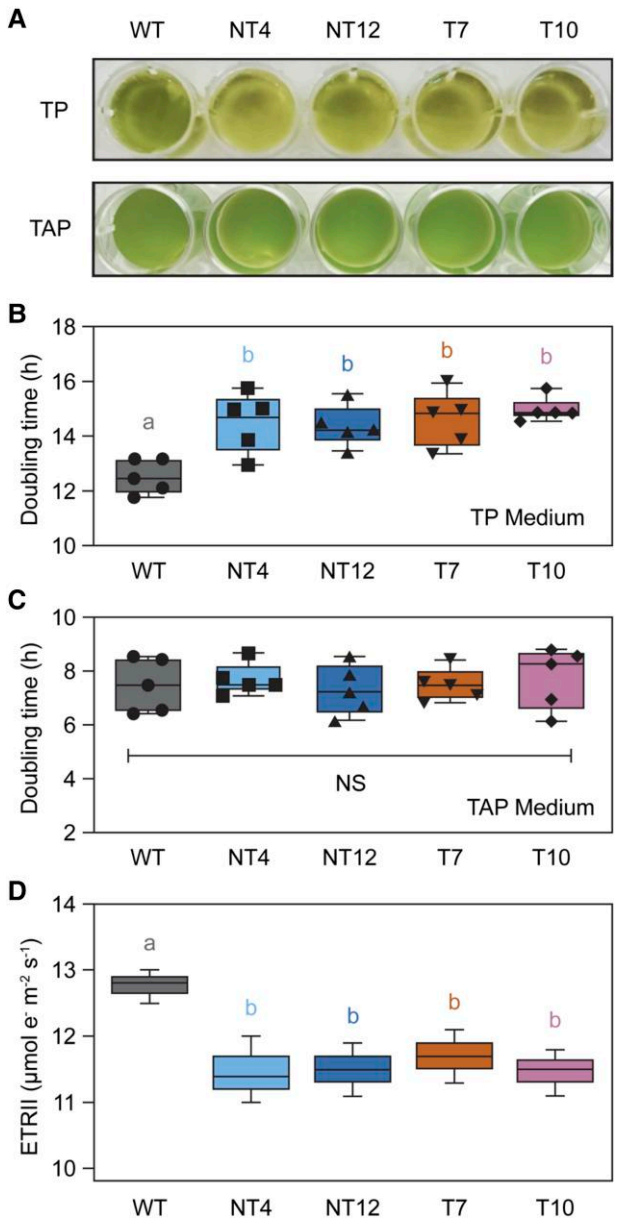

Figure 2. Growth and electron transport phenotype of chimeric PSAF-FNR mutants. **A)** Representative image of photoautotrophic (tris-phosphate [TP] medium) and photomixotrophic (tris-acetate-phosphate [TAP] medium) growth for the chimeric PSAF-FNR mutants. **B)** Average doubling time in hours for growth in TP medium. **C)** Average doubling time in hours for growth in TAP medium. For **A)** to **C)**, the growth conditions used were ~60 μmol photons m^{-2} s^{-1} (white LED) 14 h/10 h day–night cycling, shaking at 120 rpm at 20 °C. **D)** PSII electron transport rate (ETRII) determined via chlorophyll fluorescence for the WT and PSAF-FNR mutants at ~60 μmol photons m^{-2} s^{-1} in the presence of 10 mM sodium bicarbonate. Median values are plotted as the center-line in each box (n = 5), box limits are the first and third quartiles, and whiskers show the range. Means were then compared between genotypes using an ordinary 2-way ANOVA and corrected using Tukey's multiple comparison test followed by an HSD test with alpha = 0.05. Different letters indicate significant differences between data points. WT, wild-type; NT4, native/tethered line 4; NT12, native/tethered line 12; T7, tethered-only line 7; T10, tethered-only line 10.

to monomeric LHCII (band 1), trimeric LHCII (band 2), PSII (band 3), and PSI (band 4) (Fig. 3A) (Iwai et al. 2010; Takahashi et al. 2013; Buchert et al. 2018). An additional green band (band 5) was present in the gradients of both the NT12 and T7 mutants, and band 4 was also of lower intensity compared to the WT (Fig. 3A). Immunoblotting with an anti-PSAE antibody revealed the presence of PSI in bands 4 and 5 (Fig. 3B). The anti-FNR antibody confirmed a wide distribution of FNR throughout the gradient in the WT (fractions 2 to 11), consistent with previous results (Mosebach et al. 2017; Buchert et al. 2018). In contrast in NT12, both native ~35 kDa and chimeric ~53 kDa proteins were detected and were concentrated predominantly in fractions 7 to 11, with a peak in intensity similar to PSI (Fig. 3B). In the T7 mutant, only the 53 kDa chimeric protein was detected and was again largely absent from fractions 1 to 5, coinciding with PSI distribution (Fig. 3B). The position of band 5 is consistent with that previously reported for the PSI–LHCII–cytb_6f supercomplex often observed in State II in Chlamydomonas (Iwai et al. 2010; Terashima et al. 2012; Takahashi et al. 2013). However, immunoblotting for the Rieske iron–sulfur protein subunit of cytb_6f (PETC) revealed this complex was largely absent from band 5 (fraction 8) and instead concentrated in fractions 4 to 6 in both mutants (Fig. 3B). We repeated the immunoblotting for fraction 8 using anti-PETC and anti-PetA antibodies with a longer exposure compared to Fig. 3B and this uncovered the presence of cytb_6f in band 5 (Fig. 3C), though this was poorly correlated with PSI as revealed by anti-PSAE antibody, with relatively higher cytb_6f/PSI ratio in the WT compared to the mutants. In contrast, the absorption spectrum of band 5 in the mutants revealed the clear presence of additional chlorophyll b in the 470 and 650 nm regions consistent with the presence of LHCII complexes (Fig. 3D). Enhanced fluorescence emission from PSI at 720 nm relative to PSII emission at 685 nm (Fig. 3E) showed that NT12 and T7 cells adopted State II, while the WT adopted State I under growth conditions (Fig. 3E). The increased presence of LHCII, revealed by immunoblotting with the anti-LHCBM5 antibody, in fractions 7 and 8 of the NT12 and T7 mutants compared to the WT supported this assignment (Fig. 3B). Interestingly, the mutant cells also adopted State II more readily than the WT under 4 different conditions that paired high or low CO_2 with oxic or anoxic conditions (Supplementary Fig. S1A). However, the total capacity to switch to State II was similar in the WT and mutants, as verified by treating cells with nigericin which collapses ΔpH and drives cells fully to State II (Bulté et al. 1990) (Supplementary Fig. S1B). The chimeric protein therefore successfully associates with PSI, causes a redistribution of native FNR in NT12, and also results in a shift from State I to State II under normal growth conditions in both mutants.

Chimeric PSAF-FNR mutants show increased PSII and decreased PSI abundance

To assess effects on the relative abundance of key photosynthetic proteins, we performed a proteomic analysis of NT12 and T7 mutant cells compared to the WT via label-free quantitative (LFQ) mass spectrometry (MS), as previously described (Flannery et al. 2021). Proteins were extracted from whole cell lysates produced from 4 independent (biological) replicate cultures for each of the WT, NT12, and T7 lines grown under 60 μmol photons m^{-2} s^{-1} in TP medium. The biological replicates were analyzed with 3 technical repeats. The 36 MS data files were then processed for protein identification and quantification using MaxQuant (Cox and Mann 2008) to generate iBAQ abundance scores (Schwanhäusser et al. 2011) to reveal differential protein levels. Using this approach, we first normalized each iBAQ score to the intra-analysis sum of the subunit iBAQ scores from proteins of the core photosynthetic machinery: PSI, PSII, cytb_6f, and ATP synthase, as listed in Supplementary Data Set 1. Using the median of 3 technical

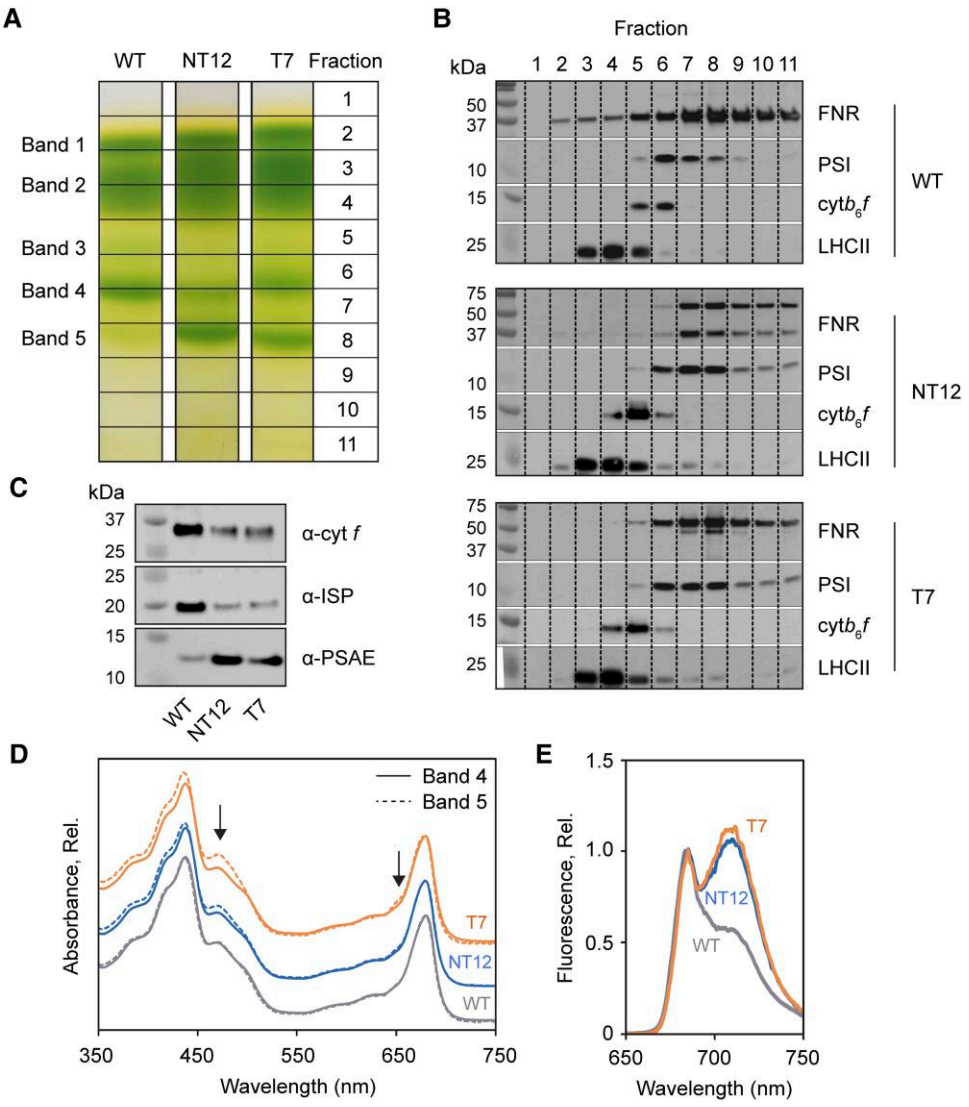

Figure 3. Localization of the PSAF-FNR chimera within PSI. **A)** Sucrose density gradients of LMNG solubilized thylakoids from WT, NT12, and T7 cells. Principle bands and fractions are numbered. **B)** Immunoblots (based on equal volume loading by sucrose gradient fraction) using anti-FNR, anti-PSAE (PSI), anti-PETC (cytb_6f), and anti-LHCBM5 (LHCII) antibodies. **C)** Immunoblots (based on equal volume loading of sucrose gradient fraction 8 alone) using anti-PetA (cyt *f*), anti-PETC (iron–sulfur protein, ISP), and anti-PSAE antibodies. **D)** Absorption spectra of bands 4 and 5 from sucrose gradients in **A)** from WT, NT12, and T7 cells, normalized to the maximum intensity at 678 nm. Black arrows indicate evidence of additional chlorophyll *b* in band 5 relative to band 4 in NT12 and T7 cells, **E)** 77K fluorescence emission spectra of WT, NT12, and T7 cells grown in TP at 60 μmol photons m^{-2} s^{-1} 14 h/10 h day–night cycling, shaking at 120 rpm. WT, wild-type; NT12, native/tethered line 12; T7, tethered-only line 7.

repeats to represent each biological replicate, we then applied a modified *t*-test incorporating permutation-based false discovery rate with 250 randomizations, as implemented in Perseus, to indicate significant differences in the abundance of selected proteins in WT vs. mutant cells. The total number of proteins identified across all 36 analyses was 4,091 (Supplementary Data Set 1). Figure 4A shows FNR and PSAF levels calculated from their individual, summed tryptic peptide ion intensities since iBAQ would be inappropriate for separate quantification of PSAF and FNR in chimeric PSAF-FNR. NT12-expressed FNR, in both native and chimeric forms combined, was produced at 3.6-fold greater abundance relative to WT. In T7, expressing only chimeric PSAF-FNR, the level of FNR was 2.4-fold greater than WT. The difference in FNR level between NT12 and T7 is consistent with the additional contribution of native FNR in NT12 to the total FNR abundance against the background of enhanced FNR expression, as PSAF-FNR, in both mutants. PSAF levels, expressed only as PSAF-FNR in the mutants, were increased, though the difference was not statistically significant (Fig. 4A). In the NT12 and T7 mutants, the abundance of PSII was increased to 1.1- to 1.2-fold relative to the WT, while the abundance of PSI decreased to 0.74- to 0.68-fold (Fig. 4B). The decrease in PSI/PSII ratio in the mutants was confirmed by comparing the electrochromic shift (ECS) signal upon a single turnover flash in the presence and absence of 3-(3,4-dichlorophenyl)-1,1-dimethylurea (DCMU) and hydroxylamine (HA) to inhibit PSII (Supplementary Fig. S2A). On the other hand, there was no significant difference in the relative abundance of PC, cytb_6f, and ATP synthase complexes in both mutants (Fig. 4B). The abundance of individual PSI subunits in the mutants followed a similar pattern to that of the whole complex for PsaA and PsaB, though for PsaC, PSAG, PSAH, PSAK, and PSAL, no significant difference could be discerned (Fig. 4C, Supplementary Fig. S3A). However, PSAD decreased to 0.76- and 0.72-fold in NT12 and T7, respectively, compared to the WT, and to 0.4- and 0.18-fold for PSAE (Fig. 4C). This decrease was corroborated by anti-PSAE immunoblots on whole cells (Supplementary Fig. S2B);

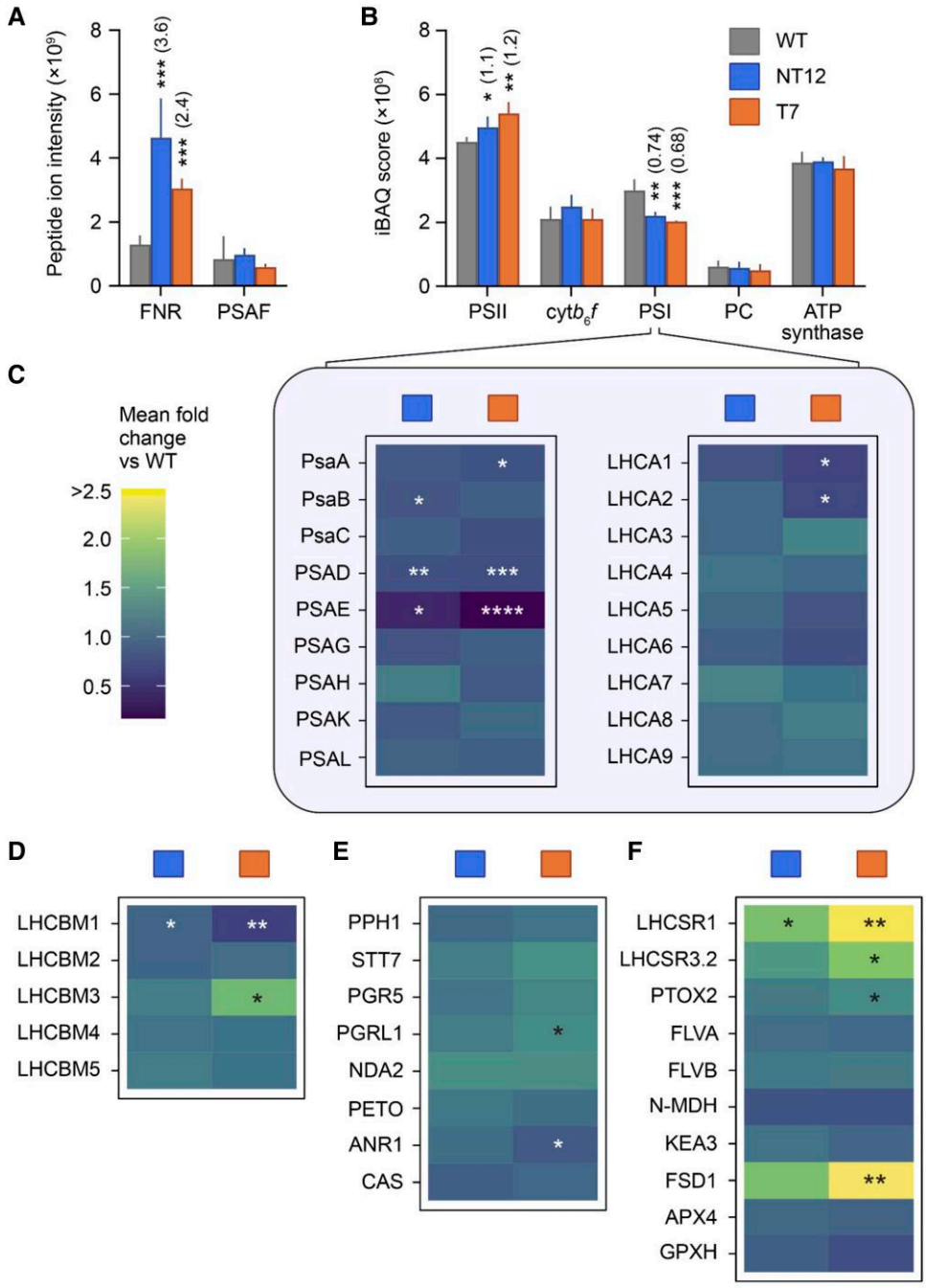

Figure 4. Quantification of proteins expressed by WT, NT12, and T7 cells. **A)** Mass spectrometry-based label-free quantification of FNR and PSAF (sum of peptide ion intensities). **B)** Intensity based absolute quantification (iBAQ) scores for photosystem II (mean of PsbA-D iBAQ scores, PSII), cytochrome b_6f (mean of subunits PetA, PetB, PETC, and PetD iBAQ scores, cytb_6f), photosystem I (mean of subunits PsaA-C, PSAD-E, PSAG-H, and PSAK-L iBAQ scores, PSI), and chloroplast ATP synthase (mean of subunits AtpA, AtpB, and ATPC iBAQ scores). **C)** Heat maps showing mean fold change vs. WT for PSI subunits and light harvesting complex I proteins (LHCA1-9). Bar charts for these proteins are shown in Supplementary Fig. S3A. **D)** State transition associated proteins: major light harvesting complex II proteins (LHCBM1-5). Bar charts for these proteins are shown in Supplementary Fig. S3B. **E)** State transition associated proteins: protein phosphatase (PPH1), serine/threonine protein kinase (STT7), and cyclic electron transport (CET) associated proteins: PGR5, PGR5-like protein 1 (PGRL1), NADH-plastoquinone reductase A2 (NDA2), cytb_6f subunit PETO, Anaerobic Response Regulator (ANR1), and calcium sensor kinase (CAS). Bar charts for these proteins are shown in Supplementary Fig. S3, C and D. **F)** stress associated proteins: LHCSR1, LHCSR3.2, plastid terminal oxidase 2 (PTOX2), flavodiiron proteins FLVA and FLVB, NADP-malate dehydrogenase (N-MDH), potassium efflux antiporter 3 (KEA3), superoxide dismutase FSD1, ascorbate peroxidase APX4, and glutathione peroxidase GPXH. Bar charts for these proteins are shown in Supplementary Fig. S3, E and F. Bars show means ± SDs of quantified proteins extracted from WT, NT12, and T7 cells. Means ± SDs for proteins in panels **C)** to **F)** are shown in Supplementary Fig. S3. q values derived from modified t-tests incorporating permutation-based false discovery rate with 250 randomizations ($n = 4$) are shown as 0.01 to 0.05*, 0.001 to 0.01**, 0.0001 to 0.001***, and <0.0001****, with exact q values listed in Supplementary Data Set 1. Fold change relative to WT is shown in parentheses in panels **A)** and **B)** for differences with $q \leq 0.05$. Differences with $q \geq 0.05$ (not significant) are not shown. WT, wild-type; NT12, native/tethered line 12; T7, tethered-only line 7.

similarly, anti-AtpB and anti-PetB (cyt b_6) supported the absence of differences in ATP synthase and cytb_6f levels. FD, which was not detected in the MS data, was instead verified by immunoblot analysis and found to be largely unchanged in the mutants (Supplementary Fig. S2B).

The PSI light harvesting proteins LHCA1-9 were detected and, of these, only LHCA1 and LHCA2 were significantly different, at 0.66-fold compared to the WT in the T7 mutant (Fig. 4C, Supplementary Fig. S3A). Of the PSII light harvesting proteins, LHCBM1 was decreased to 0.73- and 0.61-fold compared to WT in the NT12 and T7 mutants (Fig. 4D, Supplementary Fig. S3B). LHCBM2, LHCBM4, and LHCBM5 did not differ significantly in the mutants, while LHCBM3 was increased 1.7-fold in the T7 mutant but was not significantly affected in the NT12 mutant (Fig. 4D). The decrease in LHCBM1 and increase in LHCBM3 is interesting since this appears as the major phosphorylated LHCII species in the PSI–LHCI–LHCII supercomplexes (Huang et al. 2021), which are more abundant in the mutants (Fig. 3A). The state transition kinase STT7 and its cognate phosphatase PPH1 were not significantly different however (Fig. 4E, Supplementary Fig. S3C).

The CET-related proteins were also largely unaffected in the mutants, with no significant change in PGR5, NDA2, PETO, and CAS proteins observed (Fig. 4E, Supplementary Fig. S3D). Nonetheless, changes were observed in the abundance of PGRL1 and ANR1 which were increased by 1.3-fold and decreased to 0.85-fold, respectively, in only the T7 mutant (Fig. 4E). Once again, the differences in PGRL1 levels were corroborated by immunoblotting of whole cells (Supplementary Fig. S2B). Changes in the LHCSR1 photoprotective protein involved in NPQ in Chlamydomonas were also detected with levels 1.8-fold and 2.5-fold higher in NT12 and T7, respectively, while LHCSR3.2 was 1.9-fold higher in T7 (Peers et al. 2009) (Fig. 4F, Supplementary Fig. S3E). The plastid terminal oxidase (PTOX) protein involved in the photoprotective oxidation of PQ and transfer of electrons to water was also increased in the T7 mutant by 1.3-fold (Fig. 4F) (Nawrocki et al. 2018). In contrast, no significant differences were observed in the abundance of PCET proteins FLVA or FLVB or the NADPH-dependent malate dehydrogenase enzyme (N-MDH), which might be involved in reductant export from the chloroplast as in vascular plants, though direct evidence is missing in Chlamydomonas (Alric and Johnson 2017) (Fig. 4F). The putative thylakoid H^+/K^+ exchange antiporter 3 (KEA3) was also unaffected in the mutants (Fig. 4F, Supplementary Fig. S3F). However, levels of the superoxide dismutase (FSD1) were raised significantly in T7, by 2.7-fold, compared to the WT (Fig. 4F). No differences were observed between the mutants and WT of the ascorbate peroxidase (APX4) or glutathione peroxidase (GPXH) (Fig. 4F).

Of the CO_2 fixation and CCM machinery, the levels of the large and small Rubisco subunits (RbcL and RBCS) were unchanged, as was the EPYC1 linker protein which binds them into the pyrenoid (Supplementary Fig. S3G). A 1.3-fold increase in the levels of the luminal carbonic anhydrase 3 (CAH3) (Mackinder 2018) responsible for converting bicarbonate into CO_2 was observed in both mutants, while in NT12, a 1.3-fold increase in the abundance of the low carbon inducible protein 9 (LCI9) (Mackinder et al. 2017) was also seen (Supplementary Fig. S3G). The thylakoid bestrophins (BST1, BST2, and BST3) responsible for bicarbonate import across the membrane (Mukherjee et al. 2019) were all unaffected (Supplementary Fig. S3H). Among the major CBB cycle enzymes only sedoheptulose bisphosphatase levels were changed, increasing by 1.6-fold in T7 (Supplementary Fig. S3I). The major proteomic differences in the mutants therefore appear to center around altered PSI/PSII ratio and the disruption to PSAD and PSAE levels, though in the T7 cells differences are also seen in LHCII, photoprotection, CET, and CCM-related proteins.

The chimeric PSAF-FNR mutants exhibit a CO_2- and O_2-dependent electron transfer phenotype

The poorer growth on minimal TP media compared to the WT suggests an impaired ability to fix CO_2. This led us to investigate how photosynthesis and photoprotection were affected in the mutants. Chlorophyll fluorescence measurements were carried out with and without the addition of 10 mM sodium bicarbonate (i.e. high and low CO_2), and we also tested the effect of anoxic conditions. Under high CO_2/oxic conditions, the PSII quantum yield (Y(II)) was lower in the mutant cells compared to the WT below 500 μmol photons m^{-2} s^{-1}, though similar above this intensity (Fig. 5A). PSII acceptor side limitation (1-qP) was similar (Fig. 5B), while NPQ was increased significantly in the T7, T10, NT12, and NT4 mutants between 250 and 800 μmol photons m^{-2} s^{-1} compared to WT (Fig. 5, C and D). In contrast, under low CO_2/oxic conditions, Y(II) was slightly lower in NT4 and NT12 mutants, whereas 1-qP was similar compared to WT (Fig. 5, E and F). In T7 and T10, Y(II) was slightly increased compared to the WT, while 1-qP was generally lower (Fig. 5, E and F). NPQ under low CO_2/oxic conditions was significantly higher in all mutants (Fig. 5, G and H). Under high CO_2/anoxic conditions, the WT regained some slight advantage in Y(II) below 800 μmol photons m^{-2} s^{-1} compared to the mutants, with 1-qP largely similar in NT4 and NT12, but lower in T7 and T10 once again (Fig. 5, I and J). However, NPQ remained significantly higher in all the mutants at the two highest light intensities tested compared to the WT (Fig. 5, K and L). We tested whether the NPQ was of the ΔpH-dependent rapidly-relaxing qE variety by checking its relaxation in a subsequent dark period (Supplementary Fig. S4A). Under low CO_2/oxic conditions, ~65% of NPQ was of the qE type in both mutants and WT, however in high CO_2/oxic conditions, only ~50% was qE in the WT and ~20% in the mutants, consistent with a greater contribution of state transitions to the quenching (Supplementary Fig. S1A). The data suggest a CO_2 concentration-dependent phenotype with respect to NPQ, which we confirmed in the T7 mutant, with higher concentrations of CO_2 lowering the NPQ while showing less effect in the WT (Supplementary Fig. S4B). We therefore conclude that under stress conditions that were previously shown to favor CET, such as anoxia and low CO_2, the NT12, NT4, T7, and T10 mutants show an advantage in terms of NPQ generation.

The PSAF-FNR mutants show slower NADPH formation but enhanced pmf production

We next tested whether the slower photoautotrophic growth in the mutants reflected an impaired ability to reduce $NADP^+$ to NADPH due to the tethering of FNR to PSI. We investigated this by monitoring the rate of NADPH fluorescence emission rise at 330 nm provoked by illumination at 500 μmol photons m^{-2} s^{-1} of whole cells (Fig. 6A). The rate of NADPH formation was ~20% faster under anoxic conditions in the WT compared to oxic conditions, consistent with a decreased availability of oxygen as an electron acceptor (Fig. 6, B and C). However, under both oxic and anoxic conditions, the rate of NADPH formation was decreased also by ~20% in the NT12, NT4, T10, and T7 mutants compared to the wild-type (Fig. 6, B and C). Under oxic conditions in the T10 mutant and the rate of NADPH formation was also lower compared to the

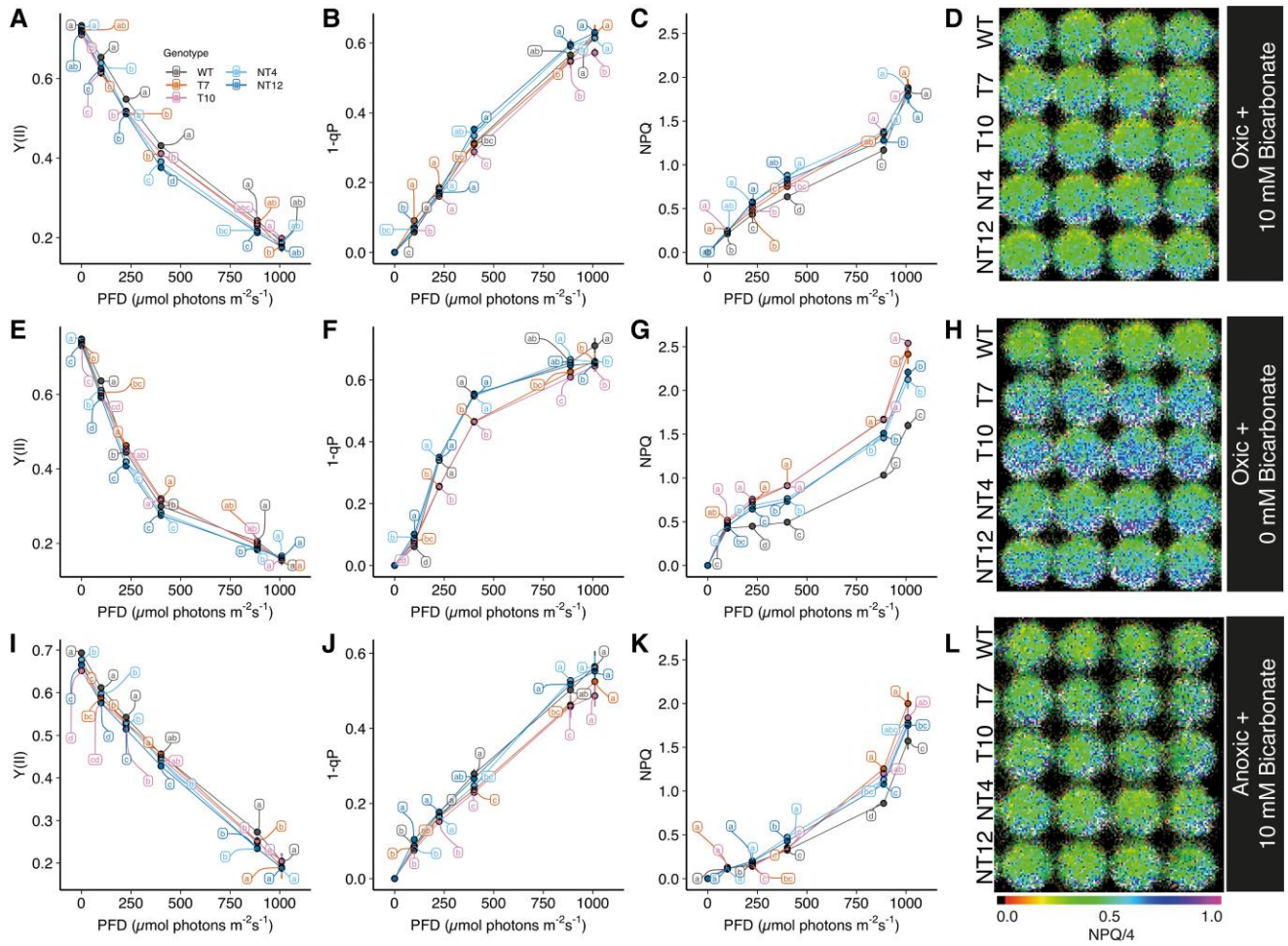

Figure 5. Comparison of light intensity, oxygen and CO_2 dependence of chlorophyll fluorescence parameters of NT12, NT4, T7, and T10 cells relative to WT. **A, E, I)** PSII quantum yield (Y(II)). **B, F, J)** Relative redox state of PSII acceptor Q_A (1-qP). **C, G, K)** Non-photochemical quenching (NPQ). **D, H, L)** Representative chlorophyll fluorescence image of NPQ in *Chlamydomonas* cells suspended in a well (NPQ is shown on a scale where the total value is divided by 4 to scale them between 0 and 1). In **A)** to **D),** oxic cells contained 10 mM $NaHCO_3$; **E)** to **H)** oxic cells without addition of $NaHCO_3$; **I)** to **L)** anoxic cells (contained glucose oxidase, catalase and covered with clear RT-qPCR film) contained 10 mM $NaHCO_3$. Error bars are SD ($n = 4$ biological replicates). Means were compared between genotypes at each light intensity using an ordinary 2-way ANOVA and corrected using Tukey's multiple comparison test followed by an HSD test with alpha = 0.05. Different letters indicate significant differences between data points at each light intensity. WT, wild-type; NT4, native/tethered line 4; NT12, native/tethered line 12; T7, tethered-only line 7; T10, tethered-only line 10.

NT4 and NT12 mutants (Fig. 6B). These data demonstrate that the rate of FD reduction of NADPH via FNR is limited in the mutants, and results in a less reduced $NADP^+$/NADPH pool (Fig. 6A). The disruption to NADPH production may therefore explain the slower photoautotrophic growth in the mutants. In principle, slower NADPH production could also prolong the lifetime of reduced FD and thus lead to enhanced acceptor side limitation and ROS generation at PSI. We tested this by examining the H_2O_2 production. In the WT and the mutants, the H_2O_2 production was higher under low CO_2 compared to high CO_2, yet the mutants produced less H_2O_2 overall than the WT under each condition (Supplementary Fig. S5).

We next tested whether the higher NPQ in the mutants could be explained by an increased generation of pmf using the ECS measurements. The amplitude of the pmf was increased in the NT12, NT4, T7, and T10 mutants at high light intensity under both high and low CO_2 and oxic and anoxic conditions compared to the WT (Fig. 7A). This pattern was also repeated under low CO_2/oxic conditions (Fig. 7B) and high CO_2 anoxic conditions (Fig. 7C) where again the mutants showed increased pmf formation at high light. Under high CO_2/anoxic conditions the overall pmf was lower consistent with the lower availability of oxygen as an electron acceptor (Fig. 7C). Under these anoxic conditions, the mutants a showed higher pmf at the higher light intensities compared to the WT (Fig. 7C). No major difference in either the relative amplitude or partitioning of the pmf components ΔpH and Δψ (membrane potential) were also observed among the WT and mutants (Supplementary Fig. S6), consistent with unchanged KEA3 levels (Fig. 4F). In principle, a higher pmf could be due to either lower proton conductivity (gH^+) as a result of downregulation of ATP synthase activity or higher proton flux across the membrane (vH^+). The gH^+ values were not significantly different in all mutants compared to the WT under each condition (Fig. 7, D to F), with the exception of slightly higher gH^+ in T7 and T10 under low CO_2/oxic conditions (Fig. 7E). Most of the difference in pmf between the WT and mutants could instead be attributed to a higher vH^+ seen at high light intensities in the mutants (Fig. 7, G to I). Collectively, these data suggest that pmf (and ΔpH) is increased due to increased proton pumping in the mutants and that this effect is most clearly seen under low CO_2 or anoxic stress.

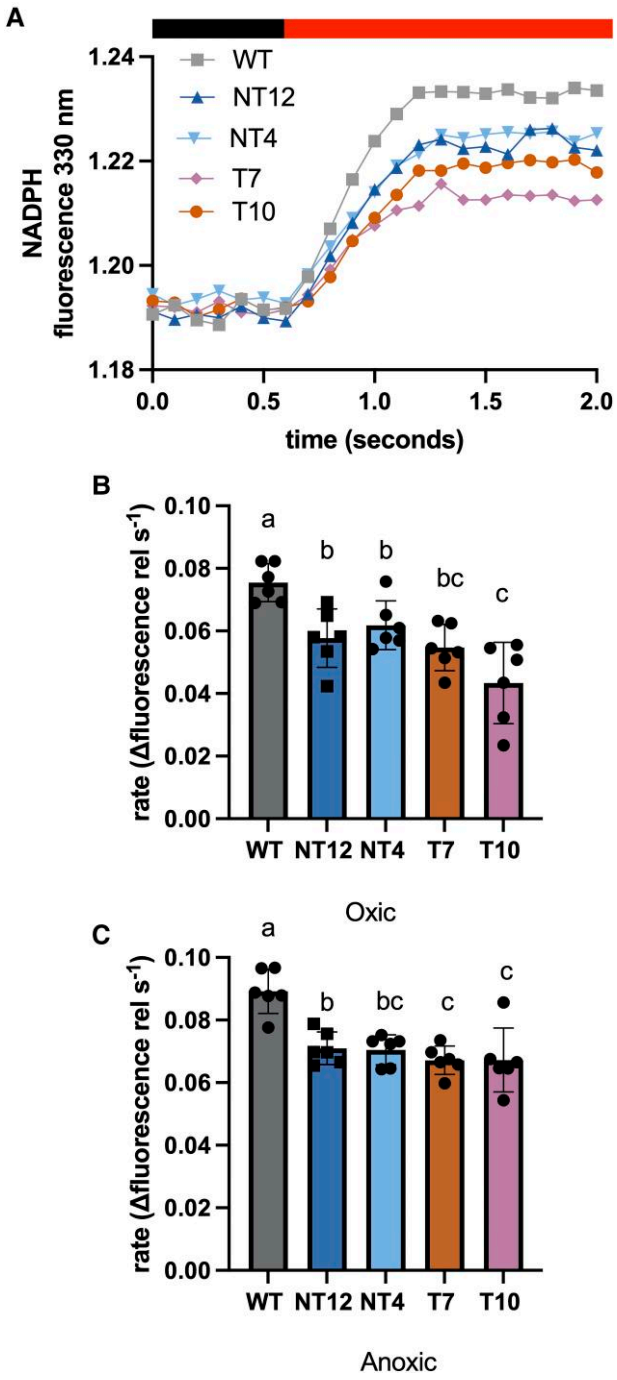

Figure 6. NADPH fluorescence parameters of NT12, NT4, T7, and T10 cells relative to WT. **A)** Representative traces showing response of NADPH fluorescence to actinic illumination. Light intensity was 550 μmol photons m^{-2} s^{-1}. Relative rate of change in NADPH fluorescence emission intensity upon illumination under **B)** high CO_2/oxic conditions and **C)** high CO_2/anoxic conditions. Error bars are SD ($n = 6$ biological replicates). Means were compared between genotypes using an ordinary 2-way ANOVA and corrected using Tukey's multiple comparison test followed by an HSD test with alpha = 0.05. Different letters indicate significant differences between data points.

The chimeric PSAF-FNR mutants show enhanced PSI acceptor side limitation and increased CET activity under anoxia

We next investigated the effect of the slower NADPH reduction rate and higher ΔpH on PSI activity in the mutants vs. WT under high CO_2/oxic conditions at 520 μmol photons m^{-2} s^{-1} (Fig. 8A). In the WT, around 35% of PSI RCs were donor-side limited (YND) and a further 62% could be photo-oxidized with a saturating pulse (YI), the remaining 3% was acceptor-side limited (YNA). In the mutants, the YI was similar to the WT, though the YNA was significantly higher and the YND significantly lower (Fig. 8A). Under high CO_2/anoxic conditions, the phenotypes of the mutants were more exaggerated with lower YND, lower YI for T7 and T10, and much higher YNA for all the mutants compared to the WT (Fig. 8B). The data are therefore consistent with the slower rate of NADPH reduction in the mutants leading to an increased acceptor side limitation of PSI, a condition made more acute by the lack of O_2 as an alternative electron acceptor. We speculated that the increased pmf and vH^+ in the mutants (Fig. 7, A to C and G to I) might reflect an unexpectedly increased capacity for CET. We tested this further by investigating PSI properties under conditions where LET is inhibited in the presence of DCMU and HA. In the presence of these inhibitors under high CO_2/oxic conditions, the rate of re-reduction of PSI in the presence of DCMU and HA at 520 μmol photons m^{-2} s^{-1} was higher in the NT12 and NT4 mutants and elevated, though not significantly so, in the T7 and T10 mutants compared to the WT (Fig. 8C). Under high CO_2/anoxic conditions, the rate of PSI reduction further increased in all cells in line with activation of CET under these conditions (Alric 2014). However, once again CET was slightly higher in the NT12, NT4 mutants, though not significantly different in T7 and T10 (Fig. 8D).

We used the ECS method to exclude the possibility that increased acceptor side limitation enhanced charge recombination in the mutants, thereby accelerating PSI re-reduction under CET conditions. We assessed the ECS decay rate in the presence of DCMU and HA to inhibit LET under high CO_2/anoxic conditions at 520 μmol photons m^{-2} s^{-1} (Fig. 9, A and B). Consistent with higher CET activity, the rate of proton flux (vH^+) was faster under anoxia in all of the mutants compared to the WT (Fig. 9B). Previously in Chlamydomonas, in vitro electron transfer from FD to the *b*-hemes in cytb_6f within the putative CET supercomplex was found to be insensitive to the inhibitor antimycin A (AA), which inhibits the PGR5 pathway in plants (Munekage et al. 2004; Iwai et al. 2010). However, recently it was shown that PGR5-dependent enhancement of *b*-heme oxidation in vivo under anoxia in Chlamydomonas is sensitive to AA (Buchert et al. 2022). If increased NPQ and pmf generation under anoxia reflect such an enhanced CET through cytb_6f, then logically they should be diminished by AA treatment. This was indeed the case with both WT and mutant NPQ and pmf generation significantly retarded by AA (Supplementary Fig. S7, A and B). However, the differences between WT and mutants were not completely eliminated by AA. The changes in NPQ and pmf were observed without significant decreases in the overall rate of measured PSII electron transfer (Supplementary Fig. S7C) indicating AA did not retard LET at these concentrations. Collectively, these data confirm that CET is unexpectedly enhanced in the mutants, explaining the higher NPQ, pmf, and vH^+ levels observed, however part of these differences is AA-insensitive suggesting a possible role for PCET in supporting CET in the mutants.

Discussion

In this study, we tested the hypothesis that FNR location determines the allocation of photosynthetic electrons between LET and CET, with binding of FNR to PSI suggested to promote LET and binding to cytb_6f promoting CET (Joliot and Johnson 2011). Using CRISPR-Cas9 gene editing, we successfully generated Chlamydomonas mutants where the FNR was tethered to the

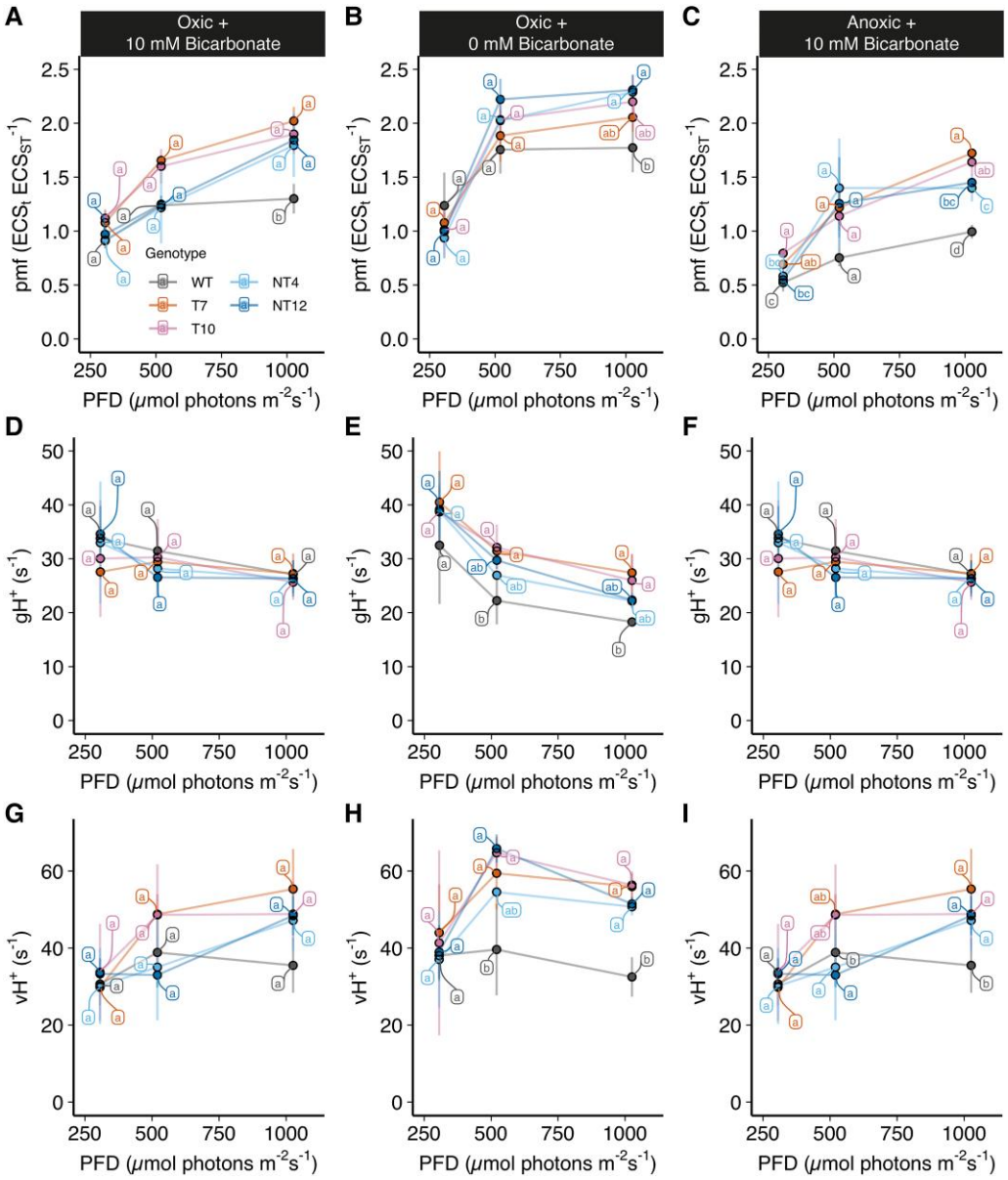

Figure 7. Comparison of ECS absorption parameters of NT12, NT4, T7, and T10 cells relative to WT. Proton motive force (pmf) under **A)** high CO_2/oxic, **B)** low CO_2/oxic, and **C)** high CO_2/anoxic conditions. Proton conductivity (gH^+) under **D)** high CO_2/oxic, **E)** low CO_2/oxic, and **F)** high CO_2/anoxic conditions. Proton flux (vH^+) under **G)** high CO_2/oxic, **H)** low CO_2/oxic, and **I)** high CO_2/anoxic conditions. Anoxia was achieved as described in Fig. 5 except that mineral oil was used. Error bars are SD ($n = 3$ biological replicates). Means were compared between genotypes using an ordinary 2-way ANOVA and corrected using Tukey's multiple comparison test followed by an HSD test with alpha = 0.05. Different letters indicate significant differences between data points at each light intensity. WT, wild-type; NT4, native/tethered line 4; NT12, native/tethered line 12; T7, tethered-only line 7; T10, tethered-only line 10.

stromal side of PSI via PSAF. As a control, we compared these tethered-only (T) mutants to both the WT and mutants which possessed both the tethered and native FNR (NT). Normally in Chlamydomonas, FNR is found loosely bound to the membrane or free, with a fraction co-migrating with PSI and some with cytb_6f (Mosebach et al. 2017; Buchert et al. 2018). Here, the chimeric PSAF-FNR protein was found to be associated with both PSI–LHCI and the larger PSI–LHCI–LHCII supercomplex following membrane solubilization and sucrose gradient ultracentrifugation (Fig. 3B). The chimeric protein appeared to be largely stable and did not undergo significant proteolytic cleavage in the mutants (Fig. 1F). We did however observe a perturbation in both the T and NT mutants in both overall levels of the PSI complex and specifically the stromal PSAD and PSAE subunits. As can be seen in Fig. 1A, the predicted position of the chimeric PSAF-FNR at the stromal face of PSI is adjacent to PSAD and PSAE and therefore it is possible that its presence may sterically inhibit their binding. The T and NT mutants showed a lower rate of photosynthetic growth and lower PSII electron transport rate at lower light intensities with higher PSI (YNA) acceptor side limitation, under high CO_2 conditions compared to the WT (Figs. 2, 5, A to C, and 8A). We traced this slower photoautotrophic growth in the mutants to a slower rate of NADPH formation, indeed the steady state amplitude of NADPH fluorescence was also lower (Fig. 6A). Interestingly, the photomixotrophic growth of the mutants on acetate, a reduced carbon source was unaffected, supporting the notion that the primary lesion in the mutants is in NADPH production.

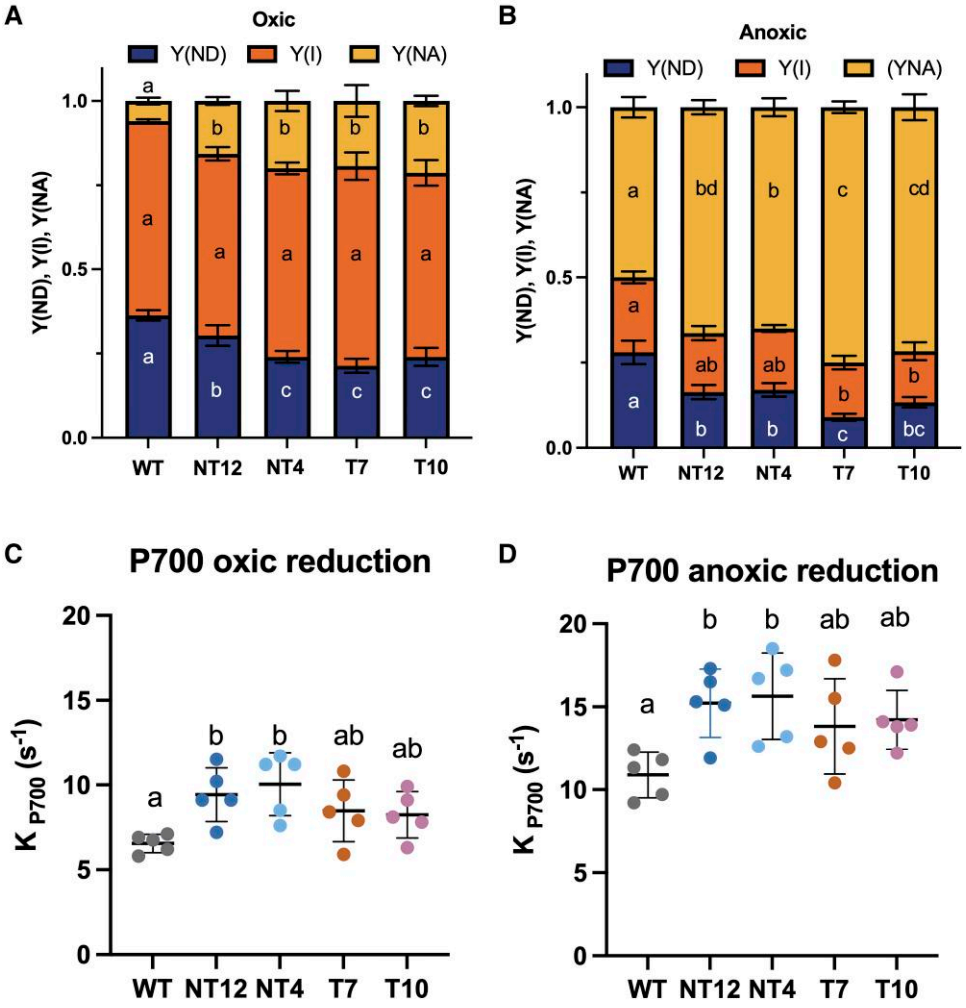

Figure 8. Comparison of PSI absorption parameters of NT12, NT4, T7, and T10 cells relative to WT. P700 redox state determined in cells subjected to 10 s illumination at 520 μmol photons m^{-2} s^{-1} red actinic light under oxic or anoxic conditions. Y(NA) = fraction of acceptor-side limited PSI, Y(ND) = fraction of donor-side limited PSI, Y(I) = fraction of photochemically active PSI in **A)** high CO_2/oxic conditions and **B)** high CO_2/anoxic conditions. The calculated first order rate constant for P700 reduction, (K_{P700}) in cells treated with 10 μM 3-(3,4-dichlorophenyl)-1,1-dimethylurea (DCMU) and 1 mM hydroxylamine (HA) and illuminated for 10 s with 520 μmol photons m^{-2} s^{-1} red actinic light in **C)** high CO_2/oxic conditions and **D)** high CO_2/anoxic conditions, respectively. Horizontal lines represent means and symbols raw data points. Error bars are SD ($n = 5$ biological replicates). Means were compared between genotypes using an ordinary 2-way ANOVA and corrected using Tukey's multiple comparison test followed by an HSD test with alpha = 0.05. Different letters indicate significant differences between genotypes. WT, wild-type; NT4, native/tethered line 4; NT12, native/tethered line 12; T7, tethered-only line 7; T10, tethered-only line 10.

How could the presence of the chimeric FNR disrupt $NADP^+$ reduction? On the stromal/acceptor side of PSI, the expected location of PSAF-FNR was adjacent to the PsaC bound terminal 4Fe4S clusters F_A and F_B involved in electron transfer to FD (Su et al. 2019; Naschberger et al. 2022). The reaction cycle of FNR requires the binding and unbinding of 2 successive FD molecules, with a reduced semiflavin storing the first electron prior to the 2-electron reduction of $NADP^+$ (Carrillo and Ceccarelli 2003). It is possible that the chimera delays the arrival of the second electron by ensuring each FNR is mostly only served by the immediately adjacent PSI or alternatively that access to the FD binding site on FNR is partly obscured. Interestingly, the distribution of the native FNR in the sucrose gradients was different in NT12 and the WT, with the former following the distribution of PSI (Fig. 3B). FNR is commonly found as a dimer, with dimerization promoted in vascular plants by TIC62 and TROL, its membrane tethers (Twachtmann et al. 2012; Kramer et al. 2021). In a similar way, it is possible that the tethering of FNR to PSAF promotes the dimerization of the native FNR with it at the membrane surface in the NT mutants, thus shifting its distribution relative to the WT (Fig. 3B). This may explain why despite the presence of additional native FNR in the NT mutants compared to the T mutants, the phenotypes with regard to $NADP^+$ reduction are similar (Fig. 7A). Slower $NADP^+$ reduction could lead to an increased lifetime for unpaired electrons on either FD or the semiflavin of FNR, potentiating formation of superoxide, which is rapidly converted to the longer-lived ROS H_2O_2 by superoxide dismutase (Foyer and Hanke 2022). Indeed, we observe enhanced levels of the superoxide dismutase in T7 mutant compared to the WT (Fig. 4F). However, this did not feed through to differences in H_2O_2 levels, which were unexpectedly lower in both low and high CO_2 conditions in the mutants compared to the WT (Supplementary Fig. S5). As seen previously for FNR overexpressors, the overall higher levels of FNR in the NT and T mutants may protect them from any ROS buildup by pre-priming antioxidant defenses (Kozuleva et al. 2016).

In contrast to the limitations observed in NADPH generation in the mutants, pmf (and ΔpH) production was unexpectedly

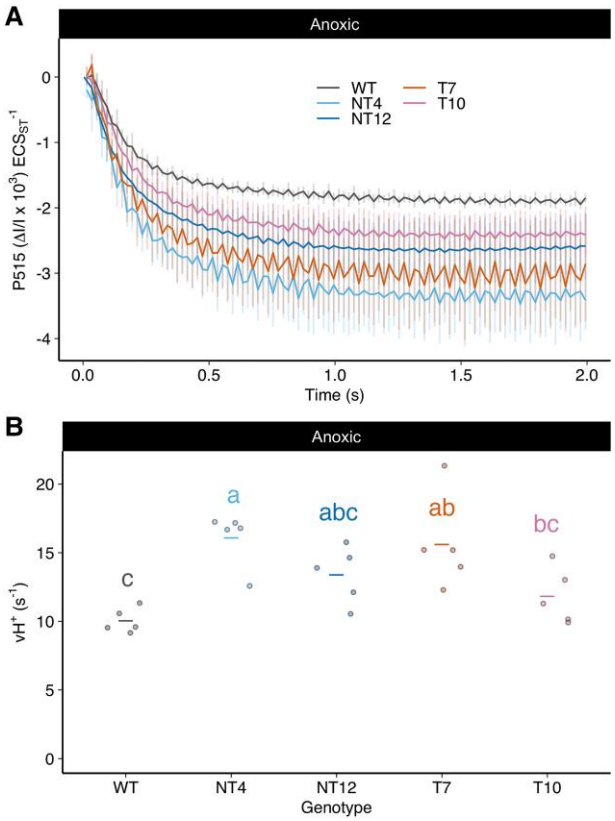

Figure 9. Rate of ECS absorption decay under CET conditions in NT12, NT4, T7, and T10 cells relative to WT. **A)** Initial rate of ECS decay in the presence of 10 μM DCMU and 1 mM HA under anoxic conditions upon cessation of a 10 s illumination period using 502 μmol photons m^{-2} s^{-1}. **B)** Calculated initial rate (vH^+) of ECS decay under the same conditions. Horizontal lines represent means and symbols raw data points Error bars are SD ($n = 4$ biological replicates). Means were compared between genotypes using an ordinary 2-way ANOVA and corrected using Tukey's multiple comparison test followed by an HSD test with alpha = 0.05. Different letters indicate significant differences between data genotypes. WT, wild-type; NT4, native/tethered line 4; NT12, native/tethered line 12; T7, tethered-only line 7; T10, tethered-only line 10.

enhanced due to increased proton-pumping (vH^+) (Fig. 7). Consistent with this, we observed higher rates of CET in the chimeric mutants by both P700 (Fig. 8, C and D) and ECS (Fig. 9, B and C) methods. In line with the increases in CET and ΔpH, we observed higher NPQ in the mutants under stress conditions (Fig. 5, G and K). The NPQ was confirmed to be of the qE type (Supplementary Fig. S4A) and it cannot be completely excluded that the higher levels of LHCSR1 and LHCSR3.2 may also contribute to this phenotype, at least in the T mutants (Fig. 4F). We found the larger pmf and NPQ under anoxia in the mutants was sensitive to AA, the inhibitor of the PGR5-dependent CET pathway (Supplementary Fig. S7, A and B). However, the difference between the WT and mutants was not completely eliminated, suggesting that either the PGR5-dependent CET pathway was only partially inhibited by AA in Chlamydomonas and/or there was enhanced electron flow through the NADPH-dependent NDA2 CET pathway in the mutants. However, since NADPH production is more limited in the mutants, this seems unlikely. Alternatively, PCET via the flavodiiron proteins, which also use reduced FD as a substrate might contribute to the increased NPQ and pmf in the mutants compared to the WT, at least under low CO_2 conditions. In most cases, the NT and T mutant lines behaved in a similar way with regard to pmf, NPQ, and CET, suggesting that the FNR phenotype of the chimera was dominant, perhaps due to the observed co-localization of native and chimeric FNR in the mutants (Fig. 3B). Despite higher pmf and NPQ, we observed lower P700 oxidation (YND) under anoxia in the chimeric mutants compared to the WT (Fig. 8). Since the fraction of pmf present as ΔpH was essentially unchanged in the mutants (Supplementary Fig. S6), consistent with unchanged KEA3 levels (Fig. 4F), this suggests that another factor is at play in suppressing YND. Saliently, a similar phenotype was recently reported for the Arabidopsis *hope2* mutant, which showed increased CET activity and normal NPQ, though higher YNA and lower YND than the WT (Degen et al. 2023). Increasing the flow of electrons to the PSI donor side via high CET may therefore mitigate the extent of any increase in YND. Alternatively, YND may require a proper poising of the NADPH pool as previously suggested (Hald et al. 2008a). Since there was no evidence for enhanced YND in the mutants, it can be ruled out that the chimera affected interaction between PC and PSI at the lumenal face of PSAF (Fig. 8A).

Although CET and state transitions can operate independently (Terashima et al. 2012; Takahashi et al. 2013), it is possible that the higher CET capacity reflects the increased shift to State II in the mutants which partitions more excitation toward PSI (Cardol et al. 2009). State II is induced by the activation of the kinase STT7 via binding of PQH_2 to the oxidizing site on the cytb_6f complex (Zito et al. 1999; Depège et al. 2003). The more reduced PQ pool (inferred by 1-qP, Fig. 5, B and F) in the mutants observed in light curves under high CO_2/oxic conditions is consistent with activation of State II under these conditions (Fig. 3E). However, consistent with recent reports (Buchert et al. 2018), we found that cytb_6f and PSI–LHCII distribution were poorly correlated (Fig. 3B), suggesting that the association between these complexes is extremely labile or it is unnecessary for CET. Alternatively, the acceleration of CET under these conditions in the mutants could be due to pleiotropic effects of the mutation on CET effector proteins. PGRL1 levels were slightly increased in T7, though not significantly in NT12. In contrast, ANR1, a putative auxiliary subunit of cytb_6f involved in CET, abundance was lower than in the WT (Takahashi et al. 2016) (Fig. 4E). A decrease was also observed in LHCA2 proteins, the absence of which was previously shown to promote CET (Terashima et al. 2012; Steinbeck et al. 2018) (Fig. 4C). As stated above, we found that PSAD and PSAE abundance is lower in the chimeric mutants. Interestingly, past work in Arabidopsis mutants lacking PSAD and PSAE shows that while PSI remains functional, the balance between LET and CET is shifted toward the latter (Hald et al. 2008b). Indeed, in both cases, CET was enhanced by around 1.5-fold compared to the WT, similar to the enhancement seen here. It is possible that loss of these subunits somehow provides easier access for electrons to the CET pathway. Given the recent reports in Arabidopsis that membrane tethered FNR promotes CET (Kramer et al. 2021; Rodriguez-Heredia et al. 2021), we suggest that the FNR chimera likewise results in more electrons being channeled into the CET (and possibly PCET) pathway at the expense of LET as summarized in Fig. 10. Such an explanation could rationalize why direct binding of FNR to cytb_6f (prevented by the chimera) is unnecessary for CET. Indeed, the decreased CET in the PGR5 mutant (Johnson et al. 2014; Buchert et al. 2020) goes along with a depletion of membrane bound FNR (Mosebach et al. 2017). Finally, it is also possible that the chimera affects the conformation of FNR in such a way as to enhance the relative rate of the back reaction (i.e. NADPH to FD) relative to $NADP^+$ reduction. These ideas now require further testing.

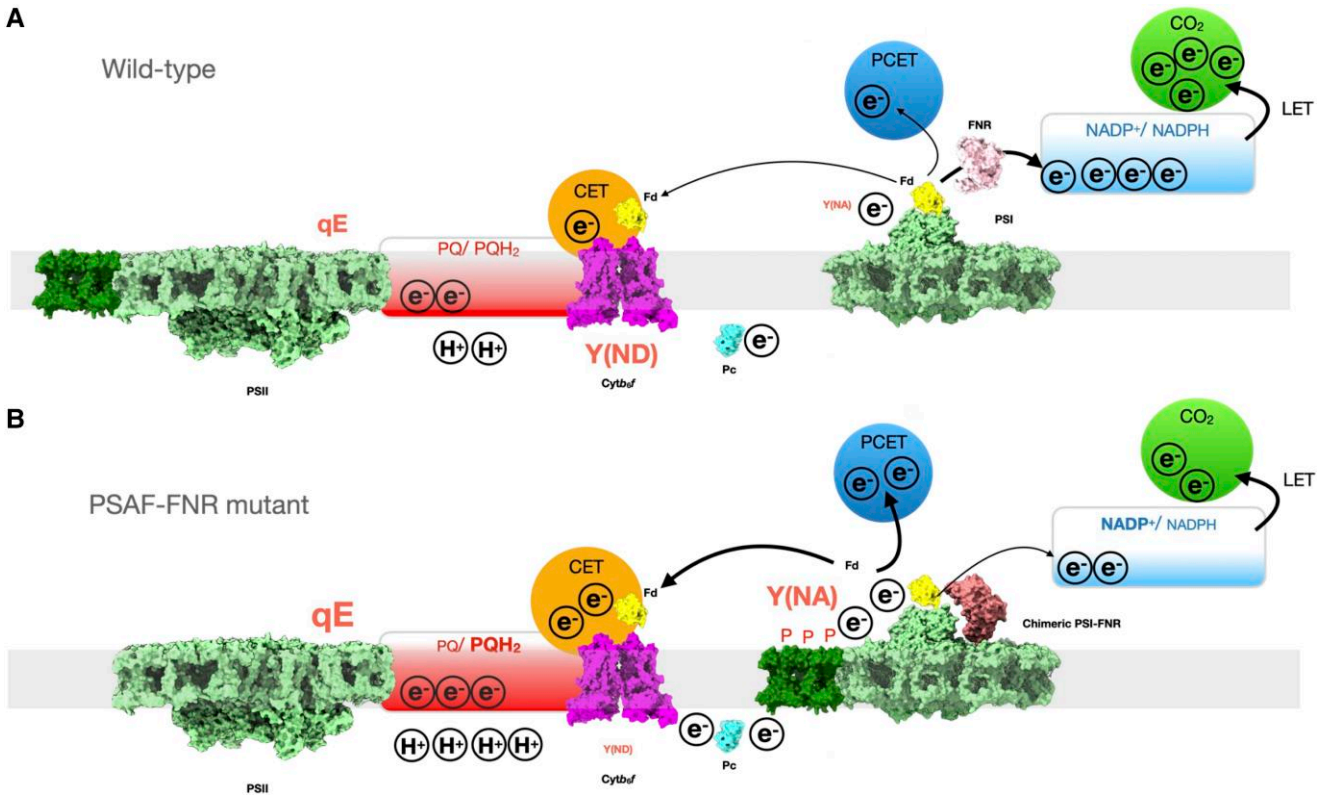

Figure 10. Schematic model outlining the effect of PSAF-FNR chimera on photosynthesis. **A)** In the wild-type, the native FNR efficiently shuttles electrons from FD to $NADP^+$ to drive LET and CO_2 fixation. Alternative electron sinks such as CET and PCET receive sufficient electrons from FD to support additional ATP synthesis for CO_2 fixation. The ΔpH and redox poise of the $NADP^+$/NADPH pool support a moderate level of qE and allow oxidation of PSI (Y(ND)). PSI acceptor side limitation (Y(NA)) is minimal. **B)** Contrastingly, in the PSAF-FNR chimeric mutants, the tethering of FNR to PSI perturbs the forward ET reaction from FD to $NADP^+$ leading to accumulation of reduced FD, increased PSI acceptor side limitation (Y(NA)), and increased PQ pool reduction, driving a transition to State II (shown by additional e^- and phosphorylation of LHCII (P)). Increased availability of reduced FD stimulates CET and likely PCET (shown by thicker arrows), increasing ΔpH which increases qE (shown by additional H^+). However, Y(ND) is not stimulated in the mutant, possibly due to loss of $NADP^+$/NADPH redox poise.

In summary, using a CRISPR-Cas9 gene editing approach, we were able to modify the location of FNR through construction of a chimera with PSAF and deletion of the native copies. This allowed us to test the hypothesis that FNR binding to PSI promotes LET over CET. Our results are inconsistent with this simple hypothesis and instead support a model where FNR location (membrane bound vs. loosely bound/free) plays a role in determining the partition of electrons between the LET and CET pathways.

Materials and methods

Strains and culturing conditions

The wild-type Chlamydomonas strain for all experiments was UVM4, kindly provided by Prof. Ralph Bock. UVM4 was generated by Neupert et al. (2009) and derives from strain CC-4350, available from the Chlamydomonas Resource Centre (https://chlamycollection.org). Cells were cultured in tris-phosphate (TP) or tris-acetate-phosphate (TAP) liquid media with revised trace elements (Kropat et al. 2011), pH 7.4, in flat bottomed flasks with 120 rpm of shaking in air at 20 °C under a 14 h/10 h day–night cycle at 60 μmol photons m^{-2} s^{-1} white LED light. All Chlamydomonas strains were maintained under low (10 to 25 μmol photons m^{-2} s^{-1}) white fluorescent light on TAP + 1.5% agar plates containing 20 μg mL^{-1} paromomycin and/or 25 μg mL^{-1} hygromycin where appropriate.

Cassette construction

The *PSAF-FNR* expression cassette was assembled into a backbone from the pLM005 vector family (Mackinder et al. 2017). The ~1.2 kbp native *PSAF* nucleotide sequence (Cre09.g412100, Phytozome v5.6) was first amplified from genomic DNA (gDNA) and inserted into pLM005 between the *PSAD* (Cre05.g238332, Phytozome v5.6) promoter + 5′UTR and terminator, downstream of the *AphVIII* cassette conferring paromomycin resistance. Next, the native *FNR* nucleotide sequence (Cre11.g476750, Phytozome v5.6) was analyzed for the presence of a chloroplast transit peptide using ChloroP (Emanuelsson et al. 1999), now renamed TargetP (Almagro Armenteros et al. 2019). A ~2.2 kbp sequence excluding the transit peptide sequence was amplified from gDNA using primers that included a 5′ linker sequence and 3′ Strep-tag II sequence, then inserted into the vector in frame with the *PSAF* sequence by restriction-ligation cloning. Lastly, a series of silent mutations were made by overlap extension PCR to remove Cas9 recognition sites in *PSAF* exon 3 and *FNR* exon 6 of the *PSAF-FNR* expression cassette. Suitable Cas9 sites were identified by searching the *C. reinhardtii* genome v5.5 using CRISPR-P 2.0 (Liu et al. 2017) and CRISPRdirect (Naito et al. 2015) and chosen due to minimal predicted off-target cleavage sites (Supplementary Table S1). Three silent mutations were made to the *PSAF* exon 3 recognition site, including removal of the PAM sequence. Codon restrictions around the *FNR* exon 6 recognition site

meant that the PAM sequence could not be modified, so 4 silent mutations were made. The final plasmid, pTE051, was sequenced to confirm correct assembly, then prepared for transformation by digestion with the blunt double-cutter Eco32I to produce the ~7 kbp *PSAF-FNR* expression cassette, shown in Fig. 1A. Sequence information is provided in Supplementary Table S1.

CRISPR-mediated mutation

CRISPR-mediated mutations were made to the Chlamydomonas nuclear genome using the Alt-R CRISPR system (Integrated DNA Technologies). The major route for DNA repair in Chlamydomonas is the nonhomologous end-joining (NHEJ) pathway, which can incorporate fragments of exogenous DNA into the breakage site during the repair process (Ghribi et al. 2020). Accordingly, to insert the *PSAF-FNR* expression cassette into the native *PSAF* gene, linearized DNA encoding the *PSAF-FNR* expression cassette (which also includes the paromomycin resistance cassette, *AphVIII*) was co-transformed into WT (UVM4) cells by electroporation with ribonucleoprotein (RNP) consisting of a modified Cas9 enzyme from *Saccharomyces pyogenes* (SpCas9) in complex with a custom single-guide RNA (sgRNA) with homology to *PSAF* exon 3. Similarly, to delete FNR, linearized DNA encoding a hygromycin resistance cassette (*AphVII*) from pLM006 (Mackinder et al. 2017) was co-transformed into NT4 and NT12 cells with RNP containing sgRNA with homology to *FNR* exon 6. sgRNA sequences were designed as mentioned above, so that only the native copies of *PSAF* or *FNR* were targeted for CRISPR-mediated cleavage, while the edited *PSAF* and *FNR* sequences in the *PSAF-FNR* expression cassette were ignored by the RNP.

Briefly, cells were grown in TAP to mid-log phase at 20 °C then incubated at 33 °C for 3 h followed by harvesting and resuspension in 120 μL MAX Efficiency Transformation Reagent for Algae (Thermo Fisher) to a concentration of 2×10^8 cells mL^{-1} in a 4 mm gap cuvette. Cuvettes were incubated in a water bath at 16 °C for 5 min prior to mixing of 500 ng linearized DNA and 61 pmol RNP and a single pulse at 0.8 kV in a MicroPulser Electoroporator (BioRad). Following transformation, cells were recovered at 33° overnight in TAP + 40 mM sucrose under low light (10 to 25 μmol photons m^{-2} s^{-1}) and 120 rpm shaking before plating. Colonies were screened by colony PCR to identify disruptions at the target locus. Primers oTE587 and 588 were used to amplify across the *PSAF* gDNA coding sequence (Fig. 1B(ii)). Primers oTE497 and 511 were used to amplify a ~1 kbp fragment from within the *PSAF-FNR* expression cassette (Fig. 1B(iii)). Primers oTE347, 348, and 024 were used in a 3-primer PCR to amplify across one of the ends of the insertion site of the *AphVII* cassette in the native FNR exon 6 sequence (Fig. 1E(iii)). Primer sequences and sgRNA details are provided in Supplementary Table S1.

Thylakoid isolation and protein purification

To prepare thylakoid membranes for sucrose gradient separation, WT and mutant cell cultures were grown in 1 L TAP medium under a 14 h/10 h day–night cycle at 60 μmol photons m^{-2} s^{-1} white LED light at 20 °C until the cells reached mid-log growth phase (2 to 4×10^6 cells mL^{-1}), the cells were then transferred to TP medium for 2 to 3 d to switch to autotrophic growth, at which point the cells were collected by centrifugation at 4,000 × *g* for 5 min. Cell pellets were washed once and resuspended in Buffer A (10 mM HEPES pH 7.5, 0.33 M sucrose, 10 mM EDTA, 10 mM NaF, 1.5 mM KCl). EDTA-free protease inhibitor tablets (Merck) and DNAse were added prior to lysis by 2 passes through a French press at 8,000 psi. The cell lysate was centrifuged at 3,000 × *g* for 10 min, 4 °C and thylakoids collected by centrifugation at 56,000 × *g*, 30 min, 4 °C. Thylakoids were washed once in Buffer B (10 mM HEPES pH 7.5, 10 mM EDTA, 1.5 mM KCl) and resuspended to a chlorophyll concentration of 1 mg mL^{-1}. Lauryl maltose neopentyl glycol (LMNG) was added to the thylakoids to a final concentration of 2% (w/v) and incubated for 30 min, 4 °C in the dark with gentle agitation. Insoluble material was pelleted at 56,000 × *g*, 30 min, 4 °C. The chlorophyll concentration across all samples was normalized and 500 μL of each loaded onto sucrose density gradients made by the freeze-thawing 10 mM HEPES pH 7.5, 0.85 M sucrose, 0.006% LMNG (w/v). The samples were centrifuged for 22 h at 288,000 × *g*, 4 °C. One milliliter fractions were collected by top-down unloading using a syringe and needle.

Electrophoresis and immunoblotting

Cell quantities were normalized to chlorophyll concentration for whole cell blots and by volume for sucrose gradient fraction blots. Proteins were extracted by boiling and sonicating for 10 min in Laemmli buffer prior to separation by SDS-PAGE and immunoblotting. SDS-PAGE and immunoblotting were carried out as previously described (Wood et al. 2018). Antibodies were obtained from Agrisera (AtpB-AS05 085; FD-AS06 121; FNR-AS15 2909; LHCBM5-AS09 408; PetA-AS06 119; PetB-AS03 034; PetC-AS08 330; PGRL1-AS19 4311; PsaE-AS22 4731) with the exception of the PsaF antibody which is described elsewhere (Hippler et al. 1997).

Low-temperature fluorescence emission spectroscopy (77 K)

WT or mutant cell cultures were diluted in TP to ~5 mg Chl mL^{-1} then frozen in liquid nitrogen and analyzed using a FluoroLog FL3-22 spectrofluorimeter (Jobin Yvon). Fluorescence emission spectra were recorded by excitation at 435 nm and monitoring between 600 and 800 nm. Spectra were normalized to the peak at 680 nm, associated with fluorescence from PSII.

Physiological measurements

For oxic conditions, cells were equalized in TP (100 μg Chl mL^{-1}) containing 15% Ficoll, then incubated in the dark for 10 min. For anoxic conditions, cells were mixed with oxygen scavengers: 50 mM glucose, 30 U mL^{-1} catalase, and 10 U mL^{-1} glucose oxidase. For high CO_2, 10 mM sodium bicarbonate was added prior to experiments, for low CO_2, no additions were made. Cells were then overlaid with 500 μL mineral oil or sealed with clear RT-qPCR film to prevent gas exchange, and cells were incubated in the dark for 40 min without shaking to deplete oxygen.

For chlorophyll fluorescence, ECS, and P700 measurements, cells were grown in TAP medium until mid-log phase under a 14 h/10 h day–night cycle at 60 μmol photons m^{-2} s^{-1}, white LEDs, 120 rpm shaking at 20 to 22 °C. Cells were then collected by centrifugation at 2,100 × *g* for 2 min, resuspended in TP medium, and returned to the above conditions for at least 24 h. For high light conditions, cells were placed under 200 μmol photons m^{-2} s^{-1} of red actinic light for 24 h using a magnetic stirrer and sodium bicarbonate was added to a final concentration of 10 mM. Prior to measurements, cells were collected via centrifugation and resuspended in 15% Ficoll (w/v) in TP.

Chlorophyll fluorescence measurements were performed using an ImagingPAM (Heinz Walz GmbH, Effeltrich, Germany). A total of 400 μL of cells (100 μg Chl mL^{-1}) resuspended in 15% Ficoll was added to each well of a 24-well plate (see figure legends for

details of treatments). Cells were dark-adapted for 10 min prior to Fm determination using an 800 ms saturating pulse. Light curves and induction curves were performed according to the description in the figures.

ECS measurements were performed using the DualPAM (Heinz Walz GmbH, Effeltrich, Germany) with the P515 emitter/detector module. A total of 1 mL of cells (33 μg Chl mL^{-1}) in 15% Ficoll was added to a quartz cuvette, which was placed in the sample holder so that the emitter head could be lowered into the cuvette. Cells were dark-adapted for 5 min prior to measurements for oxic conditions and 35 min for anoxic conditions, as detailed in the figure legends. Proton motive force was calculated from the decay of the P515 signal when red actinic light was turned off by fitting a single exponential decay to the first 300 ms in the dark to determine the span of the signal decay (ECS_t). The proton conductance (gH^+) was calculated as the inverse of the rate constant of this decay. Proton flux (vH^+) was calculated as $ECS_t \times gH^+$. P700 oxidation was measured in a similar way using a DualKLAS (Heinz Walz GmbH, Effeltrich, Germany).

Decay of P700 oxidation (WL 840 to 965 nm) was measured after 10 s of red actinic light illumination at 502 μmol photons m^{-2} s^{-1}. At the end of the illumination period, a saturating 200 ms multiple turnover flash was used to determine maximum P700 oxidation (Pm) and the first 1.5 s was used to fit a nonlinear decay function for calculation of K (100 μg Chl mL^{-1}) were dark-adapted prior to measurements with 10 μM DCMU + 1 mM HA.

NADPH fluorescence

NADPH fluorescence was measured at 460 nm with 10 nm slit width (excitation 340 nm, 5 nm slit width), integration time 0.01 s. Actinic illumination was provided by a Schott KL 1500 HAL light source with 610 nm long pass filter. Samples were illuminated for 30 s followed by 60 s of dark. Rates were calculated using a linear fit over the time in which the light was turned on or off, or during the illumination period. Fifteen samples were taken for each condition from 3 biological replicates.

H_2O_2 assay

For H_2O_2 quantification, cells were grown as described above and 1 mL of TP culture was then diluted at a 1:1 ratio with fresh TP medium, containing 1 U of horseradish peroxidase and 5 μM of Amplex Red (ThermoFisher) and incubated for 1 h under growth conditions. Cells were removed by centrifugation and the fluorescence intensity of oxidized Amplex Red (resorufin) was immediately quantified using a BMG Labtech Plate Reader Excitation/Emission 560/580-10 nm and compared against a linear H_2O_2 standard.

MS

Cells (WT, NT12, and T7 strains) were grown in TAP liquid medium as 4 independent replicate cultures. At mid-log phase (1 to 5×10^6 cells mL^{-1}), the cells were transferred to TP medium for 2 to 3 d to switch to autotrophic growth. Cells were harvested by centrifugation in 5 mL aliquots at 1,200 × g for 2 min and the pellets flash frozen in liquid N_2 before storage at −80 °C. Cell pellets (1 per analysis) were suspended in 20 μL 2% (w/v) Na dodecylsulphate, 40 mM Tris base, 60 mM dithiothreitol (DTT) (lysis buffer) and solubilized by bead beating with an equal volume of 0.5 mm silica–zirconia beads at 95 °C (Krynická et al. 2019). The cell lysates were recovered after brief centrifugation and the beads washed with 50 μL lysis buffer which was then combined with the primary lysate. Proteins were extracted from the lysates by precipitation using a 2D clean-up kit (Cytiva) according to the manufacturer's protocol and the pellets solubilized in 90 μL 4% (w/v) Na deoxycholate, 100 mM Tris-HCl, pH 8.5 (Duan et al. 2024). After reduction (10 mM DTT, 56 °C, 5 min) and S-methylthiolation (20 mM S-methyl methanethiosulfonate, room temperature, 10 min), proteins were digested with 1 μg premixed trypsin/endoproteinase Lys-C (Promega) at 37 °C for 16 h with shaking at 800 rpm. Peptides were isolated after precipitating the deoxycholate by adding absolute acetonitrile to 20% (v/v) and 10% (v/v) trifluoroacetic acid (TFA) to 0.5% (v/v). After dilution to 5% (v/v) acetonitrile with 3 vol 0.5% (v/v) TFA, peptides were desalted using C18 spin columns (Thermo Fisher Scientific) according to the manufacturer's instructions and dried in a vacuum concentrator.

Quantitative proteomic analysis by nano-flow liquid chromatography coupled to mass spectrometry (nanoLC-MS) was performed using the Vanquish Neo/Exploris 480 system (Thermo Fisher Scientific) with acquisition parameters as previously described (Flannery et al. 2021) except that a 2-h gradient and 20 dependent scans were selected. Protein identification and label-free quantification (LFQ) were performed by searching the MS data files against the *C. reinhardtii* reference proteome database (https://www.uniprot.org/proteomes/UP000006906, downloaded on October 3, 2023 and edited to include the FNR-PsaF chimeric protein sequence) using MaxQuant v. 1.6.10.43 (Cox and Mann 2008). For LFQ, the iBAQ (Schwanhäusser et al. 2011) and "match between runs" options were selected and the output was configured for export into Microsoft Excel and GraphPad Prism v. 10.2.2 using Perseus v. 2.0.10.0 (Tyanova et al. 2016).

Statistical analysis

Information on the proteomic LFQ data is provided in Supplementary Data Set 1.

Statistical analysis for other figures is provided in Supplementary Table S2.

Accession numbers

Sequence data from this article can be found in the GenBank data library under the accession number PV240273.

Accession numbers for major proteins described in this study are listed in Supplementary Table S3. Accession numbers for all proteins detected by MS in this study are listed in Supplementary Data Set 1.

Acknowledgments

The authors wish to thank Professor Ralph Bock, Max Planck Institute of Molecular Plant Physiology, for the gift of the UVM4 strain and Dr. Trong Khoa Pham, biOMICS Facility of the Faculty of Science Mass Spectrometry Centre at the University of Sheffield, for conducting the nanoLC-MS and MaxQuant analyses.

Author contributions

T.Z.E.-M., M.S.P., and G.E.D. performed the majority of the research and analyzed the data. P.J.J., K.H.R., F.R.H., and F.B. performed additional experiments. T.Z.E.-M., M.S.P., G.E.D., C.N.H., A.H., L.C.M.M., M.H., and M.P.J. conceived the experiments and wrote the manuscript. All authors read and approved the manuscript prior to submission. T.Z.E.-M., M.S.P., and G.E.D. contributed equally to the manuscript. All authors agreed that they can list the paper as Emrich-Mills et al., Proctor et al., or Degen et al. for the purpose of their CVs.

Supplementary data

The following materials are available in the online version of this article.

Supplementary Figure S1. 77K fluorescence emission spectra of WT, NT12, and T7 cells illuminated with 420 nm light.

Supplementary Figure S2. ECS and immunoblot quantification of key proteins expressed in WT, NT12, and T7 cells.

Supplementary Figure S3. Additional mass spectrometry quantification of proteins expressed in WT, NT12, and T7 cells.

Supplementary Figure S4. Effect of added sodium bicarbonate on NPQ in oxic cells.

Supplementary Figure S5. Partitioning of the proton motive force into ΔpH and Δψ.

Supplementary Figure S6. Hydrogen peroxide levels in WT, NT12, and T7 cells.

Supplementary Figure S7. Effect of antimycin A on chlorophyll fluorescence and ECS parameters in WT, NT12, and T7 cells under anoxia with 10 mM $NaHCO_3$.

Supplementary Table S1. Plasmid, sgRNA, and primer sequence information.

Supplementary Table S2. Statistical analysis for all figures and supplementary figures.

Supplementary Table S3. Accession numbers.

Supplementary Data Set 1. Mass spectrometry source data.

Funding

M.P.J. acknowledges funding from the Leverhulme Trust grants RPG-2019-045 and RPG-2021-345. M.P.J. also acknowledges financial support from the Biotechnology and Biological Sciences Research Council (BBSRC UK), award number BB/V006630/1. T.Z.E.-M. was supported by a BBSRC White Rose DTP studentship in Mechanistic Biology. F.R.H. was supported by a Diamond PhD studentship. C.N.H. is supported by a European Research Council Synergy award 854126. M.H. was supported by the DFG (Deutsche Forschungsgemeinschaft) [grant number HI 739/13-3] and DFG FOR 5573—GoPMF [grant number HI 739/25-1].

Conflict of interest statement. None declared.

Data availability

The mass spectrometry proteomics data have been deposited to the ProteomeXchange Consortium via the PRIDE partner repository (http://proteomecentral.proteomexchange.org) with the data set identifier PXD052753. All other data can be obtained from the corresponding author upon request.

References

Almagro Armenteros JJ, Salvatore M, Emanuelsson O, Winther O, von Heijne G, Elofsson A, Nielsen H. Detecting sequence signals in targeting peptides using deep learning. *Life Sci Alliance*. 2019:2(5): e201900429. https://doi.org/10.26508/lsa.201900429

Alric J. Redox and ATP control of photosynthetic cyclic electron flow in *Chlamydomonas reinhardtii* (II) involvement of the PGR5–PGRL1 pathway under anaerobic conditions. *Biochim Biophys Acta Bioenerg*. 2014:1837(6):825–834. https://doi.org/10.1016/j.bbabio.2014.01.024

Alric J, Johnson X. Alternative electron transport pathways in photosynthesis: a confluence of regulation. *Curr Opin Plant Biol*. 2017:37: 78–86. https://doi.org/10.1016/j.pbi.2017.03.014

Alric J, Lavergne J, Rappaport F. Redox and ATP control of photosynthetic cyclic electron flow in *Chlamydomonas reinhardtii* (I) aerobic conditions. *Biochim Biophys Acta Bioenerg*. 2010:1797(1):44–51. https://doi.org/10.1016/j.bbabio.2009.07.009

Bojko M, Kruk J, Więckowski S. Plastoquinones are effectively reduced by ferredoxin:NADP$^+$ oxidoreductase in the presence of sodium cholate micelles. Significance for cyclic electron transport and chlororespiration. *Phytochemistry*. 2003:64(6):1055–1060. https://doi.org/10.1016/s0031-9422(03)00506-5

Buchert F, Hamon M, Gäbelein P, Scholz M, Hippler M, Wollman F-A. The labile interactions of cyclic electron flow effector proteins. *J Biol Chem*. 2018:293(45):17559–17573. https://doi.org/10.1074/jbc.ra118.004475

Buchert F, Mosebach L, Gäbelein P, Hippler M. PGR5 is required for efficient Q cycle in the cytochrome b_6f complex during cyclic electron flow. *Biochem J*. 2020:477(9):1631–1650. https://doi.org/10.1042/bcj20190914

Buchert F, Scholz M, Hippler M. Electron transfer via cytochrome b_6f complex displays sensitivity to antimycin A upon STT7 kinase activation. *Biochem J*. 2022:479(1):111–127. https://doi.org/10.1042/bcj20210802

Bulté L, Gans P, Rebéillé F, Wollman F-A. ATP control on state transitions in vivo in *Chlamydomonas reinhardtii*. *Biochim Biophys Acta Bioenerg*. 1990:1020(1):72–80. https://doi.org/10.1016/0005-2728(90)90095-l

Burlacot A. Quantifying the roles of algal photosynthetic electron pathways: a milestone towards photosynthetic robustness. *New Phytol*. 2023:240(6):2197–2203. https://doi.org/10.1111/nph.19328

Burlacot A, Dao O, Auroy P, Cuiné S, Li-Beisson Y, Peltier G. Alternative photosynthesis pathways drive the algal CO_2-concentrating mechanism. *Nature*. 2022:605(7909):366–371. https://doi.org/10.1038/s41586-022-04662-9

Cardol P, Alric J, Girard-Bascou J, Franck F, Wollman F-A, FinazziG. Impaired respiration discloses the physiological significance of state transitions in Chlamydomonas. *Proc Natl Acad Sci U S A*. 2009:106(37):15979–15984. https://doi.org/10.1073/pnas.0908111106

Cariti F, Chazaux M, Lefebvre-Legendre L, Longoni P, Ghysels B, Johnson X, Goldschmidt-Clermont M. Regulation of light harvesting in *Chlamydomonas reinhardtii* two protein phosphatases are involved in state transitions. *Plant Physiol*. 2020:183(4):1749–1764. https://doi.org/10.1104/pp.20.00384

Carrillo N, Ceccarelli EA. Open questions in ferredoxin-NADP$^+$ reductase catalytic mechanism. *Eur J Biochem*. 2003:270(9):1900–1915. https://doi.org/10.1046/j.1432-1033.2003.03566.x

Chaux F, Burlacot A, Mekhalfi M, Auroy P, Blangy S, Richaud P, Peltier G. Flavodiiron proteins promote fast and transient O_2 photoreduction in Chlamydomonas. *Plant Physiol*. 2017:174(3):1825–1836. https://doi.org/10.1104/pp.17.00421

Clowez S, Godaux D, Cardol P, Wollman F-A, Rappaport F. The involvement of hydrogen-producing and ATP-dependent NADPH-consuming pathways in setting the redox poise in the chloroplast of *Chlamydomonas reinhardtii* in anoxia. *J Biol Chem*. 2015:290(13): 8666–8676. https://doi.org/10.1074/jbc.m114.632588

Cox J, Mann M. MaxQuant enables high peptide identification rates, individualized p.p.b.-range mass accuracies and proteome-wide protein quantification. *Nat Biotechnol*. 2008:26(12):1367–1372. https://doi.org/10.1038/nbt.1511

DalCorso G, Pesaresi P, Masiero S, Aseeva E, Schünemann D, Finazzi G, Joliot P, Barbato R, Leister D. A complex containing PGRL1 and PGR5 is involved in the switch between linear and cyclic electron flow in Arabidopsis. *Cell*. 2008:132(2):273–285. https://doi.org/10.1016/j.cell.2007.12.028

Dang K-V, Plet J, Tolleter D, Jokel M, Cuiné S, Carrier P, Auroy P, Richaud P, Johnson X, Alric J, et al. Combined increases in mitochondrial cooperation and oxygen photoreduction compensate for deficiency in cyclic electron flow in *Chlamydomonas reinhardtii*. *Plant Cell*. 2014:26(7):3036–3050. https://doi.org/10.1105/tpc.114.126375

Degen GE, Jackson PJ, Proctor MS, Zoulias N, Casson SA, Johnson MP. High cyclic electron transfer via the PGR5 pathway in the absence of photosynthetic control. *Plant Physiol*. 2023:192(1):370–386. https://doi.org/10.1093/plphys/kiad084

Degen GE, Johnson MP. Photosynthetic control at the cytochrome b_6f complex. *Plant Cell*. 2024:36(10):4065–4079. https://doi.org/10.1093/plcell/koae133

Depège N, Bellafiore S, Rochaix J-D. Role of chloroplast protein kinase Stt7 in LHCII phosphorylation and state transition in Chlamydomonas. *Science*. 2003:299(5612):1572–1575. https://doi.org/10.1126/science.1081397

Desplats C, Mus F, Cuiné S, Billon E, Cournac L, Peltier G. Characterization of Nda2, a plastoquinone-reducing type II NAD(P)H dehydrogenase in Chlamydomonas chloroplasts. *J Biol Chem*. 2009:284(7):4148–4157. https://doi.org/10.1074/jbc.m804546200

Duan X, Zhang Y, Huang X, Ma X, Gao H, Wang Y, Xiao Z, Huang C, Wang Z, Li B, et al. GreenPhos, a universal method for in-depth measurement of plant phosphoproteomes with high quantitative reproducibility. *Mol Plant*. 2024:17(1):199–213. https://doi.org/10.1016/j.molp.2023.11.010

Emanuelsson O, Nielsen H, von Heijne G. Chlorop, a neural network-based method for predicting chloroplast transit peptides and their cleavage sites. *Protein Sci*. 1999:8(5):978–984. https://doi.org/10.1110/ps.8.5.978

Flannery SE, Hepworth C, Wood WHJ, Pastorelli F, Hunter CN, Dickman MJ, Jackson PJ, Johnson MP. Developmental acclimation of the thylakoid proteome to light intensity in Arabidopsis. *Plant J*. 2021:105(1):223–244. https://doi.org/10.1111/tpj.15053

Foyer CH, Hanke G. ROS production and signalling in chloroplasts: cornerstones and evolving concepts. *Plant J*. 2022:111(3):642–661. https://doi.org/10.1111/tpj.15856

Ghribi M, Nouemssi SB, Meddeb-Mouelhi F, Desgagné-Penix I. Genome editing by CRISPR-Cas: a game change in the genetic manipulation of Chlamydomonas. *Life*. 2020:10(11):295. https://doi.org/10.3390/life10110295

Hald S, Nandha B, Gallois P, Johnson GN. Feedback regulation of photosynthetic electron transport by NADP(H) redox poise. *Biochim Biophys Acta Bioenerg*. 2008a:1777(5):433–440. https://doi.org/10.1016/j.bbabio.2008.02.007

Hald S, Pribil M, Leister D, Gallois P, Johnson GN. Competition between linear and cyclic electron flow in plants deficient in photosystem I. *Biochim Biophys Acta Bioenerg*. 2008b:1777(9):1173–1183. https://doi.org/10.1016/j.bbabio.2008.04.041

Hippler M, Drepper F, Farah J, Rochaix J-D. Fast electron transfer from cytochrome c6 and plastocyanin to photosystem I of *Chlamydomonas reinhardtii* requires PsaF. *Biochemistry*. 1997:36(21):6343–6349. https://doi.org/10.1021/bi970082c

Huang Z, Shen L, Wang W, Mao Z, Yi X, Kuang T, Shen J-R, Zhang X, Han G. Structure of photosystem I–LHCI–LHCII from the green alga *Chlamydomonas reinhardtii* in state 2. *Nat Commun*. 2021:12(1):1100. https://doi.org/10.1038/s41467-021-21362-6

Iwai M, Takizawa K, Tokutsu R, Okamuro A, Takahashi Y, Minagawa J. Isolation of the elusive supercomplex that drives cyclic electron flow in photosynthesis. *Nature*. 2010:464(7292):1210–1213. https://doi.org/10.1038/nature08885

Johnson X, Alric J. Interaction between starch breakdown, acetate assimilation, and photosynthetic cyclic electron flow in *Chlamydomonas reinhardtii*. *J Biol Chem*. 2012:287(31):26445–26452. https://doi.org/10.1074/jbc.m112.370205

Johnson X, Steinbeck J, Dent RM, Takahashi H, Richaud P, Ozawa S-I, Houille-Vernes L, Petroutsos D, Rappaport F, Grossman AR, et al. Proton gradient regulation 5-mediated cyclic electron flow under ATP- or redox-limited conditions: a study of ΔATPase pgr5 and ΔrbcL pgr5 mutants in the green alga *Chlamydomonas reinhardtii*. *Plant Physiol*. 2014:165(1):438–452. https://doi.org/10.1104/pp.113.233593

Joliot P, Johnson GN. Regulation of cyclic and linear electron flow in higher plants. *Proc Natl Acad Sci U S A*. 2011:108(32):13317–13322. https://doi.org/10.1073/pnas.1110189108

Kozuleva M, Goss T, Twachtmann M, Rudi K, Trapka J, Selinski J, Ivanov B, Garapati P, Steinhoff H-J, Hase T, et al. Ferredoxin: NADP(H) oxidoreductase abundance and location influences redox poise and stress tolerance. *Plant Physiol*. 2016:172(3):1480–1493. https://doi.org/10.1104/pp.16.01084

Kramer M, Rodriguez-Heredia M, Saccon F, Mosebach L, Twachtmann M, Krieger-Liszkay A, Duffy C, Knell RJ, Finazzi G, Hanke GT. Regulation of photosynthetic electron flow on dark to light transition by ferredoxin:NADP(H) oxidoreductase interactions. *eLife*. 2021:10:e56088. https://doi.org/10.7554/elife.56088

Kropat J, Hong-Hermesdorf A, Casero D, Ent P, Castruita M, Pellegrini M, Merchant SS, Malasarn D. A revised mineral nutrient supplement increases biomass and growth rate in *Chlamydomonas reinhardtii*. *Plant J*. 2011:66(5):770–780. https://doi.org/10.1111/j.1365-313x.2011.04537.x

Krynická V, Georg J, Jackson PJ, Dickman MJ, Hunter CN, Futschik ME, Hess WR, Komenda J. Depletion of the FtsH1/3 proteolytic complex suppresses the nutrient stress response in the cyanobacterium *Synechocystis* sp strain PCC 6803. *Plant Cell*. 2019:31(12):2912–2928. https://doi.org/10.1105/tpc.19.00411

Kühlbrandt W. Structure and mechanisms of F-type ATP synthases. *Annu Rev Biochem*. 2019:88(1):1–35. https://doi.org/10.1146/annurev-biochem-013118-110903

Li X, Zhang R, Patena W, Gang SS, Blum SR, Ivanova N, Yue R, Robertson JM, Lefebvre PA, Fitz-Gibbon ST, et al. An indexed, mapped mutant library enables reverse genetics studies of biological processes in *Chlamydomonas reinhardtii*. *Plant Cell*. 2016:28(2):367–387. https://doi.org/10.1105/tpc.15.00465

Liu H, Ding Y, Zhou Y, Jin W, Xie K, Chen L-L. CRISPR-P 2.0: an improved CRISPR-Cas9 tool for genome editing in plants. *Mol Plant*. 2017:10(3):530–532. https://doi.org/10.1016/j.molp.2017.01.003

Lucker B, Kramer DM. Regulation of cyclic electron flow in *Chlamydomonas reinhardtii* under fluctuating carbon availability. *Photosynth Res*. 2013:117(1–3):449–459. https://doi.org/10.1007/s11120-013-9932-0

Mackinder LCM. The Chlamydomonas CO_2-concentrating mechanism and its potential for engineering photosynthesis in plants. *New Phytol*. 2018:217(1):54–61. https://doi.org/10.1111/nph.14749

Mackinder LCM, Chen C, Leib RD, Patena W, Blum SR, Rodman M, Ramundo S, Adams CM, Jonikas MC. A spatial interactome reveals the protein organization of the algal CO_2-concentrating mechanism. *Cell*. 2017:171(1):133–147.e14. https://doi.org/10.1016/j.cell.2017.08.044

Malone LA, Proctor MS, Hitchcock A, Hunter CN, Johnson MP. Cytochrome b_6f—orchestrator of photosynthetic electron transfer. *Biochim Biophys Acta Bioenerg*. 2021:1862(5):148380. https://doi.org/10.1016/j.bbabio.2021.148380

Mosebach L, Heilmann C, Mutoh R, Gäbelein P, Steinbeck J, Happe T, Ikegami T, Hanke G, Kurisu G, Hippler M. Association of

ferredoxin:NADP$^+$ oxidoreductase with the photosynthetic apparatus modulates electron transfer in *Chlamydomonas reinhardtii*. *Photosynth Res*. 2017:134(3):291–306. https://doi.org/10.1007/s11120-017-0408-5

Mukherjee A, Lau CS, Walker CE, Rai AK, Prejean CI, Yates G, Emrich-Mills T, Lemoine SG, Vinyard DJ, Mackinder LCM, et al. Thylakoid localized bestrophin-like proteins are essential for the CO_2 concentrating mechanism of *Chlamydomonas reinhardtii*. *Proc Natl Acad Sci U S A*. 2019:116(34):16915–16920. https://doi.org/10.1073/pnas.1909706116

Munekage Y, Hashimoto M, Miyake C, Tomizawa K-I, Endo T, Tasaka M, Shikanai T. Cyclic electron flow around photosystem I is essential for photosynthesis. *Nature*. 2004:429(6991):579–582. https://doi.org/10.1038/nature02598

Murchie EH, Ruban AV. Dynamic non-photochemical quenching in plants: from molecular mechanism to productivity. *Plant J*. 2020:101(4):885–896. https://doi.org/10.1111/tpj.14601

Naito Y, Hino K, Bono H, Ui-Tei K. CRISPRdirect: software for designing CRISPR/Cas guide RNA with reduced off-target sites. *Bioinformatics*. 2015:31(7):1120–1123. https://doi.org/10.1093/bioinformatics/btu743

Naschberger A, Mosebach L, Tobiasson V, Kuhlgert S, Scholz M, Perez-Boerema A, Ho TTH, Vidal-Meireles A, Takahashi Y, Hippler M, et al. Algal photosystem I dimer and high-resolution model of PSI-plastocyanin complex. *Nat Plants*. 2022:8(10):1191–1201. https://doi.org/10.1038/s41477-022-01253-4

Nawrocki WJ, Bailleul B, Cardol P, Rappaport F, Wollman F-A, Joliot P. Maximal cyclic electron flow rate is independent of PGRL1 in Chlamydomonas. *Biochim Biophys Acta Bioenerg*. 2019a:1860(5):425–432. https://doi.org/10.1016/j.bbabio.2019.01.004

Nawrocki WJ, Bailleul B, Picot D, Cardol P, Rappaport F, Wollman F-A, Joliot P. The mechanism of cyclic electron flow. *Biochim Biophys Acta Bioenerg*. 2019b:1860(5):433–438. https://doi.org/10.1016/j.bbabio.2018.12.005

Nawrocki WJ, Buchert F, Joliot P, Rappaport F, Bailleul B, Wollman F-A. Chlororespiration controls growth under intermittent light. *Plant Physiol*. 2018:179(2):630–639. https://doi.org/10.1104/pp.18.01213

Nawrocki WJ, Santabarbara S, Mosebach L, Wollman F-A, Rappaport F. State transitions redistribute rather than dissipate energy between the two photosystems in Chlamydomonas. *Nat Plants*. 2015:2(4):16031. https://doi.org/10.1038/nplants.2016.31

Nelson N, Junge W. Structure and energy transfer in photosystems of oxygenic photosynthesis. *Annu Rev Biochem*. 2015:84(1):1–25. https://doi.org/10.1146/annurev-biochem-092914-041942

Neupert J, Karcher D, Bock R. Generation of Chlamydomonas strains that efficiently express nuclear transgenes. *Plant J*. 2009:57(6):1140–1150. https://doi.org/10.1111/j.1365-313x.2008.03746.x

Peers G, Truong TB, Ostendorf E, Busch A, Elrad D, Grossman AR, Hippler M, Niyogi KK. An ancient light-harvesting protein is critical for the regulation of algal photosynthesis. *Nature*. 2009:462(7272):518–521. https://doi.org/10.1038/nature08587

Rodriguez-Heredia M, Saccon F, Wilson S, Finazzi G, Ruban AV, Hanke GT. Protection of photosystem I during sudden light stress depends on ferredoxin:NADP(H) reductase abundance and interactions. *Plant Physiol*. 2021:188(2):1028–1042. https://doi.org/10.1093/plphys/kiab550

Rühle T, Dann M, Reiter B, Schünemann D, Naranjo B, Penzler J-F, Kleine T, Leister D. PGRL2 triggers degradation of PGR5 in the absence of PGRL1. *Nat Commun*. 2021:12(1):3941. https://doi.org/10.1038/s41467-021-24107-7

Schwanhäusser B, Busse D, Li N, Dittmar G, Schuchhardt J, Wolf J, Chen W, Selbach M. Global quantification of mammalian gene expression control. *Nature*. 2011:473(7347):337–342. https://doi.org/10.1038/nature10098

Setif P, Shimakawa G, Kriegar-Liszkay A, Miyake C. Identification of the electron donor to flavodiiron proteins in *Synechocystis* sp. PCC 6803 by in vivo spectroscopy. *Biochim Biophys Acta Bioenerg*. 2020:1861(10):148256. https://doi.org/10.1016/j.bbabio.2020.148256

Steinbeck J, Ross IL, Rothnagel R, Gäbelein P, Schulze S, Giles N, Ali R, Drysdale R, Sierecki E, Gambin Y, et al. Structure of a PSI–LHCI–cyt b_6f supercomplex in *Chlamydomonas reinhardtii* promoting cyclic electron flow under anaerobic conditions. *Proc Natl Acad Sci U S A*. 2018:115(41):10517–10522. https://doi.org/10.1073/pnas.1809973115

Su X, Ma J, Pan X, Zhao X, Chang W, Liu Z, Zhang X, Li M. Antenna arrangement and energy transfer pathways of a green algal photosystem-I–LHCI supercomplex. *Nat Plants*. 2019:5(3):273–281. https://doi.org/10.1038/s41477-019-0380-5

Takahashi H, Clowez S, Wollman F-A, Vallon O, Rappaport F. Cyclic electron flow is redox-controlled but independent of state transition. *Nat Commun*. 2013:4(1):1954. https://doi.org/10.1038/ncomms2954

Takahashi H, Schmollinger S, Lee J-H, Schroda M, Rappaport F, Wollman F-A, Vallon O. PETO interacts with other effectors of cyclic electron flow in Chlamydomonas. *Mol Plant*. 2016:9(4):558–568. https://doi.org/10.1016/j.molp.2015.12.017

Terashima M, Petroutsos D, Hüdig M, Tolstygina I, Trompelt K, Gäbelein P, Fufezan C, Kudla J, Weinl S, Finazzi G, et al. Calcium-dependent regulation of cyclic photosynthetic electron transfer by a CAS, ANR1, and PGRL1 complex. *Proc Natl Acad Sci U S A*. 2012:109(43):17717–17722. https://doi.org/10.1073/pnas.1207118109

Terauchi AM, Lu S-F, Zaffagnini M, Tappa S, Hirasawa M, Tripathy JN, Knaff DB, Farmer PJ, Lemaire SD, Hase T, et al. Pattern of expression and substrate specificity of chloroplast ferredoxins from *Chlamydomonas reinhardtii*. *J Biol Chem*. 2009:284(38):25867–25878. https://doi.org/10.1074/jbc.m109.023622

Tolleter D, Ghysels B, Alric J, Petroutsos D, Tolstygina I, Krawietz D, Happe T, Auroy P, Adriano J-M, Beyly A, et al. Control of hydrogen photoproduction by the proton gradient generated by cyclic electron flow in *Chlamydomonas reinhardtii*. *Plant Cell*. 2011:23(7):2619–2630. https://doi.org/10.1105/tpc.111.086876

Twachtmann M, Altmann B, Muraki N, Voss I, Okutani S, Kurisu G, Hase T, Hanke GT. N-terminal structure of maize ferredoxin:NADP$^+$ reductase determines recruitment into different thylakoid membrane complexes. *Plant Cell*. 2012:24(7):2979–2991. https://doi.org/10.1105/tpc.111.094532

Tyanova S, Temu T, Sinitcyn P, Carlson A, Hein MY, Geiger T, Mann M, Cox J. The Perseus computational platform for comprehensive analysis of (prote)omics data. *Nat Methods*. 2016:13(9):731–740. https://doi.org/10.1038/nmeth.3901

Wood WHJ, MacGregor-Chatwin C, Barnett SFH, Mayneord GE, Huang X, Hobbs JK, Hunter CN, Johnson MP. Dynamic thylakoid stacking regulates the balance between linear and cyclic photosynthetic electron transfer. *Nat Plants*. 2018:4(2):116–127. https://doi.org/10.1038/s41477-017-0092-7

Yamori W, Shikanai T. Physiological functions of cyclic electron transport around photosystem I in sustaining photosynthesis and plant growth. *Annu Rev Plant Biol*. 2015:67(1):1–26. https://doi.org/10.1146/annurev-arplant-043015-112002

Zito F, Finazzi G, Delosme R, Nitschke W, Picot D, Wollman F-A. The Qo site of cytochrome b_6f complexes controls the activation of the LHCII kinase. *EMBO J*. 1999:18(11):2961–2969. https://doi.org/10.1093/emboj/18.11.2961